Nanotechnology for Environmental Engineering (2026) 11:86
https://doi.org/10.1007/s41204-026-00576-3

ORIGINAL PAPER

Plant-mediated synthesis of gold nanoparticles from *Virola oleifera* resin: optimization, characterization and cytotoxicity evaluation

Rafaella de Resende Marques[1] · Marcelo Raul Romero Tappin[2] · Licinio Fontoura[2] · Virginia Garcia Correia[2] · Marcio Soares[2] · Daniel Adesse[3,4] · Ana Maria Percebom Sette da Silva[5] · Franccesca Fornasier[6] · Mariana Gisbert Jardim dos Santos[5] · Tommaso Del Rosso[5] · Rachel Ann Hauser-Davis[1] · Enrico Mendes Saggioro[1]

Received: 12 March 2026 / Accepted: 1 June 2026 / Published online: 20 June 2026
© The Author(s) 2026

Abstract

Plant-mediated green synthesis has emerged as a sustainable and cost-effective strategy for the production of gold nanoparticles (AuNPs). In this study, gold nanoparticles were synthesized using an aqueous extract of *Virola oleifera* resin (AuNPs-Vo), and their synthesis parameters were optimized through factorial experimental design, followed by physicochemical characterization and cytotoxicity assessment. Factorial experimental designs were applied to identify optimal conditions for obtaining stable, concentrated, and monodisperse nanoparticles, evaluating extract concentration, pH, temperature, reaction time, and agitation. The plant extract was characterized by High-Performance Liquid Chromatography coupled with Ultraviolet–Visible Detection (HPLC-UV/Vis) and Liquid Chromatography–Mass Spectrometry (LC-MS), while the nanoparticles were analyzed by UV-Vis (Ultraviolet–Visible Spectroscopy), Transmission Electron Microscopy (TEM), Inductively Coupled Plasma Optical Emission Spectroscopy (ICP-OES), Dynamic Light Scattering (DLS), zeta potential, and Raman spectroscopy. Nanoparticle stability was evaluated through flocculation assays under different pH, temperature, and ionic strength values. Cytotoxicity was assessed in Vero cells employing 3-(4,5-dimethylthiazol-2-yl)-2,5-diphenyltetrazolium bromide (MTT) assays after exposure to three AuNPs-Vo concentrations and their precursors (extract and $HAuCl_4$), along with the analysis of oxidative stress biomarkers: Reduced Glutathione (GSH), Glutathione S-transferase (GST), Hydrogen Peroxide (H_2O_2), Catalase (CAT), Malondialdehyde (MDA), Protein Carbonyl (PTC or Carb) and Total Antioxidant Capacity (CAOT). The most influential synthesis parameters were pH, reaction time, and extract concentration, with optimal conditions (about concentration and size) at pH 8.3, 6 minutes, and 1.0 mg mL^{-1}, respectively. Polyphenols, polyols, and flavones were identified as key agents for the reduction and stabilization of Au^{3+}. The AuNPs-Vo presented an average gold concentration of 21 mg L^{-1}, predominantly spherical morphology, particle sizes of 15–21 nm, negative surface charge, and high stability at pH 3–9. Cytotoxicity assays demonstrated high cell viability (> 85%) and no significant induction of oxidative stress ($p > 0.05$), indicating low toxicity compared to precursor reagents. In some exposures to AuNPs-Vo, there was a significant decrease in carbonylated proteins (approximately 50%). These findings highlight the potential of phytochemicals derived from Virola oleifera as sustainable reducing agents for the production of stable compounds with promising applications.

Keywords Antioxidant activity · Biocompatibility · Cytotoxicity · Green chemistry · Gold Nanoparticle · Plant-based nanomaterial · *Virola oleifera*

Introduction

Gold nanoparticles (AuNPs) are nanometric materials with dimensions on the order of one billionth of a meter (1 nm = 10^{-9} m) [23]. These compounds are chemically inert, and generally non-toxic, with physicochemical properties, such as size and shape, that can be precisely controlled [53]. Although a variety of chemical and physical methods are available for AuNP synthesis, many of these approaches exhibit limitations, including high production costs, the use

Extended author information available on the last page of the article

of toxic solvents, substantial energy demands, and the generation of hazardous by-products that pose environmental concerns [5]. In this context, plant-mediated green synthesis has emerged as a sustainable and cost-effective alternative for AuNP production [3]. Plant extracts are rich in bioactive compounds capable of acting simultaneously as reducing and stabilizing agents during nanoparticle formation [80]. In this sense, secondary plant metabolites play key roles in plant metabolism and exhibit a wide range of biological activities in animal systems [22]. Moreover, many possess strong antioxidant properties, and are chemically classified into three main groups, namely phenolic compounds, terpenes, and nitrogen-containing alkaloids [39].

Plant-derived materials, including flowers, roots, stems, and fruits, have been increasingly employed in green synthesis strategies, using extracts prepared with different solvents, *i.e.,* aqueous [64], ethanolic [43], and hexanoic solutions [8]. A major advantage of green chemistry approaches is the ability to control nanoparticle size by adjusting extract concentrations, eliminating the need for surfactants, stabilizers, or other chemical agents [27]. Despite these benefits, green synthesis methods often yield nanoparticles with certain limitations, including polydispersity, reduced stability, and limited compatibility with human physiological systems [2]. Therefore, the development of standardized and reproducible protocols is essential to obtain nanoparticles with homogeneous size and shape [56]. This can be achieved by carefully controlling synthesis parameters such as temperature, reaction time, extract concentration, pH, and agitation [9]. In this regard, statistical experimental designs, particularly factorial planning, have been proven a powerful tool for identifying the key variables that influence nanoparticle synthesis [82, 56] for example, applied a factorial design to synthesize AuNPs using a coffee (*Coffea arabica*) extract, achieving controlled and reproducible nanoparticle formation. Similarly, Valotto et al. [83] optimized AuNP synthesis using a pomegranate (*Punica granatum*) extract through factorial methodology, systematically evaluating the effects of temperature, reaction time, agitation, and extract concentration on particle size, shape, dispersion, and concentration. In addition, Contreras et al. [26] employed a factorial design to establish optimal conditions for synthesizing AuNPs from bicuíba (*Virola oleifera*) ensuring nanoparticle stability and monodispersity.

Green-synthesized AuNPs have demonstrated promising outcomes in cytotoxicity assays using animal cell models. For example, murine fibroblasts (L929) and human keratinocytes (HaCaT) exposed to AuNPs synthesized with *V. oleifera* extract displayed cell death below 40% across all tested concentrations (900–62.5 μg mL^{-1}) [29]. Similarly, low cytotoxicity was observed in the J774A.1 macrophage cell line exposed to citrate-reduced AuNPs capped with the same extract at concentrations ranging from 0.0019 to 0.1250 mg mL^{-1} [31]. In another study, Silva et al. [79] reported 100% cell viability in L929 and HaCaT cells treated with cellulose nanofibers functionalized with AuNPs synthesized from a pomegranate extract at concentrations between 2.67 and 42.7 μg mL^{-1}. In addition, AuNPs reduced with a bottlebrush (*Callistemon citrinus*) seed extract in HeLa cells led to no significant reduction in cell viability (89.66 ± 1.55%),[91] while AuNPs synthesized from a durian (*Durio zibethinus*) extract exhibit anticoagulant activity while preserving erythrocyte morphology in goat, sheep, and human models, indicating low cellular toxicity [85].

Among medicinal plants, *V. oleifera* (Myristicaceae) has attracted considerable attention due to its pronounced antioxidant properties, which have been demonstrated in several oxidative stress models [27]. This tree, commonly known in Brazil as "bicuíba," is native to South American tropical forests, particularly within the Atlantic Forest and Amazon regions [39]. Its resin has been shown to protect murine models from contrast-induced nephropathy by reducing oxidative stress and apoptosis in glomerular and tubular renal cells [14]. Additionally, it exhibits gastroprotective activity in ethanol/HCl^- and indomethacin-induced ulcer models and enhances chemotherapeutic responses in tumor cells by promoting G2/M cell cycle arrest and apoptosis [67]. These pharmacological effects are attributed to the presence of bioactive compounds such as phenolic acids, tannins, flavonoids, ferulic acid, gallic acid, quercetin, epicatechin, and eriodictyol [14, 28].

Although plant-mediated synthesis of gold nanoparticles has been widely explored as an environmentally friendly alternative to conventional chemical routes, several challenges remain, particularly regarding the reproducibility of synthesis conditions, the identification of phytochemicals involved in metal reduction, and the evaluation of nanoparticle biocompatibility. Previous studies have demonstrated that extracts from *Virola oleifera* possess high antioxidant capacity and contain phenolic compounds capable of acting as reducing agents, suggesting their potential for nanoparticle synthesis [37, 62]. In addition, earlier investigations reported the formation of gold nanoparticles using extracts from this species and indicated promising physicochemical properties and low cytotoxicity in cell models [26, 60]. However, these studies have generally focused on nanoparticle production without systematically integrating synthesis optimization, detailed phytochemical characterization, and biological safety assessment. In this context, the present study advances current knowledge by combining factorial experimental design to determine the most influential parameters for nanoparticle formation with comprehensive chemical characterization of *V. oleifera* resin and evaluation of cytotoxicity and oxidative stress responses in mammalian

cells. By linking extract composition, optimized synthesis conditions, and biological responses, this work contributes to improving the reproducibility, mechanistic understanding, and biomedical potential of plant-mediated gold nanoparticle synthesis.

Methodology

Material preparation

Virola oleifera resin sampling and preparation

Virola oleifera resin was collected during the summer season on December 2, 2023, in Afonso Cláudio, Rio da Cobra, Espírito Santo, Brazil (S20°13′49.0″; W41°06′69.2″). The source tree was taxonomically identified by the Natural Products Laboratory belonging to the Vila Velha University, and a voucher specimen (VIES 19648) was deposited at the Espírito Santo Federal University herbarium. All procedures were conducted in accordance with Brazilian environmental legislation and authorized under IEMA permit no. 629/09, in compliance with Resolution no. 29 (06/12/2007) (IEMA, 2007, 2009), which exempts special authorization for plant material collection when the tested material is essentially identical to the raw source, according to Provisional Measure nº. 2,186-16 [72]. This research involving access to Brazilian genetic heritage was registered in the SisGen under registration number A250678,). Resin extraction was carried out by performing controlled incisions in the tree trunk, allowing the resin to exude naturally. The exuded resin was then collected using sterile 10 mL plastic syringes and immediately transferred to amber bottles stored in a cooled container with ice for transportation to the laboratory. Upon arrival, the resin was vacuum filtered through a nitrocellulose membrane and autoclaved to eliminate potential contaminants. The filtered resin was then aliquoted into Petri dishes and dried in an oven at 50 °C for 24 h. The resulting dried material was ground using a porcelain crucible and stored in sterile polypropylene microtubes under refrigeration and protected from light until preparation of the aqueous extract.

AuNPs-Vo synthesis based on factorial experimental design

The AuNPs preparation was guided by a complete factorial experimental design, according to Contreras et al. [26]. The independent variables were evaluated at lower and upper levels: aqueous extract concentration (0.5–1.5 mg mL^{-1}), reaction time (6–12 min), pH (4.3 [natural]–8.3), agitation (200–400 rpm), and temperature (6–12 °C). This approach aimed to verify whether the optimal synthesis conditions remained consistent with those previously reported, considering that plant metabolism—and consequently resin composition—may vary spatially and temporally, as noted by Keijok et al., [56]. Nanoparticle synthesis was performed using a chloroauric acid ($HAuCl_4$) solution (2.5×10^{-4} mol L^{-1}) and an aqueous *V. oleifera* resin extract in a fixed 7:3 (v/v) ratio, based on prior optimization studies (Ferreira, 2016).

The statistical analyses were performed using na analysis of variance (ANOVA) applied to the factorial design to evaluate the significance of the independent variables and their interactions on nanoparticle synthesis. Effects were assessed by the F-test at a 95% confidence level ($p < 0.05$). Model adequacy was evaluated through the coefficient of determination (R^2), adjusted R^2, and residual analysis. All statistical analyses were performed using Statistica 10.0 software (StatSoft Inc., Tulsa, OK, USA). The response variables considered for optimization were maximum absorbance (Abs.max.), wavelength at maximum absorbance (λmax.), full width at half maximum (FWHM), and area under the curve (AUC), used as indicators of synthesis yield, particle size distribution, shape homogeneity, and aggregation profile.

Based on the results obtained from the complete factorial design, only statistically significant variables were selected to construct a new optimized factorial design in order to refine the synthesis conditions and obtain nanoparticles with improved physicochemical characteristics. Response surface and contour plots were generated to visualize factor interactions and identify the experimental region associated with the most favorable synthesis conditions.

Aqueous extracts were prepared at room temperature by accurately weighing the ground resin and dissolving it in ultrapure water in 5 mL volumetric flasks. The pH was adjusted using 0.1 mol L^{-1} NaOH solution. For each synthesis, 7 mL of the $HAuCl_4$ solution were transferred to a 50 mL beaker protected from light with aluminum foil, followed by the slow addition of 3 mL of the *V. oleifera* extract under continuous stirring on a hot plate. The resulting NPs were purified through five washing cycles, each consisting of centrifugation at 14,000 rpm for 20 min, removal of the supernatant, and resuspension of the precipitate in ultrapure water to the original volume. All syntheses were performed in triplicate and analyzed by UV–Vis spectrophotometry (UV-M51, Bel) in the 200–800 nm wavelength range.

Virola oleifera resin characterization

High-performance liquid chromatography analysis

A Shimadzu high-performance liquid chromatograph (HPLC) was used, equipped with a diode array detector

(DAD) model SPD-M20A, a quaternary pump model LC-20ADXR, a degasser model DGU-20A5R, an autosampler model SIL-30AC, a column oven model CTO-20AC, and a controller model CBM-20A. Data acquisition and analysis were performed using LabSolutions software (Shimadzu). All solvents were filtered through 0.2 µm membranes and consisted of Type I water, HPLC-grade trifluoroacetic acid (TEDIA), and HPLC-grade acetonitrile (Merck).

Chromatographic conditions included an ACE 3 µm C18-PFP column (150 × 3.0 mm), a flow rate of 0.6 mL min^{-1}, a column temperature of 40 °C, and detection at 232 and 280 nm. The mobile phase consisted of 0.1% trifluoroacetic acid (channel A) and acetonitrile (channel B), operated in gradient mode at times 0, 2, 15, 16, 19, 24, 27 and 35 minutes – chanel A (%): 95, 95, 80, 80, 10 and 10; chanel B (%): 5, 5, 20, 20, 90, 90, 5 and 5, in respective times. The samples were dissolved in water at 1.0 mg mL^{-1} and filtered through a 0.22 µm PVDF membrane. An injection volume of 20 µL was used.

Ultra-high-performance liquid chromatography coupled to mass spectrometry (UHPLC–MS) analysis

An ultra-high-performance liquid chromatograph (UHPLC) manufactured by Shimadzu was used, equipped with a diode array detector (DAD) model SPD-M20A, a quaternary pump model LC-30AD, a degasser model DGU-20A5, an autosampler model SIL-30AC, a column oven model CTO-30A, and a controller model CBM-20A. All solvents were filtered through 0.2 µm membranes, were Type I water, HPLC-grade formic acid (Sigma), and HPLC-grade acetonitrile (Merck). Mass spectrometric analysis was performed using a Bruker Compact mass spectrometer with the following settings: endplate offset voltage of 500 V, capillary voltage of 4500 V, nebulizer pressure of 4.0 bar, gas flow rate of 10 L min^{-1}, and source temperature of 250 °C.

Chromatographic separation was carried out using an Acquity C18 HSS PFP column (150 × 2.1 mm, 1.8 µm particle size), with a flow rate of 0.4 mL min^{-1}, a column temperature of 40 °C, and detection at 232 and 280 nm. The mobile phase consisted of 0.1% formic acid (channel A) and acetonitrile (channel B), operated in gradient mode at 0, 1, 7.35, 7.85, 9.30, 11.80, 13.20 and 17.20 minutes – – channel A (%): 95, 95, 80, 80, 10 and 10; channel B (%): 5, 5, 20, 20, 90, 90, 5 and 5, in respective times. The sample concentration was 1.0 mg mL^{-1}, and the injection volume was 5 µL.

The acquired spectra were curated using the Global Natural Products Social Molecular Networking (GNPS) platform [75]. The MS/MS data were converted to the .mzML format using ProteoWizard (MSConvert v. 3.0.24338) and subsequently processed in MZmine (v. 2.53). The resulting feature tables, along with the converted .mzML files, were uploaded to the GNPS platform [75]. Standard parameters for high-resolution data were applied for both feature-based processing and molecular network construction. The resulting network was downloaded and visualized using Cytoscape (v. 3.10.2).

Virola oleifera AuNPs-Vo characterization

UV–Vis spectroscopy analyses

Gold nanoparticle syntheses were analyzed in triplicate using UV–Visible spectroscopy (UV-M51, Bel, São Paulo, Brazil) with a spectral resolution of 1 nm over a wavelength range of 4-200–800 nm. This technique is based on the characteristic localized surface plasmon resonance (LSPR) phenomenon, whereby the reduction of gold salts leads to a visible color change from yellow to red [49]. The maximum of plasmonic resonance bands peak typically occurs between 500 and 600 nm, depending on nanoparticle size ($\Delta\lambda$) [77]. The aqueous extract was also analyzed under the same conditions for spectral comparison with the synthesized nanoparticles.

To estimate the approximate concentration of extract compounds that participated in nanoparticle formation, aqueous extract solutions at concentrations of 0.125, 0.25, 0.5, 1.0, and 2.0 mg mL^{-1} were analyzed at 277 nm. A calibration curve was constructed from these measurements (Graphic S1). Subsequently, the supernatants obtained after washing the AuNPs–Vo were analyzed at the same wavelength. The corresponding absorbance values were substituted into the calibration equation (Equation S1), and the amount of extract compound involved in nanoparticle synthesis was determined by subtracting the absorbance of the supernatant from that of the aqueous extract used under optimized synthesis conditions identified through factorial design (Equation S2).

Transmission Electron Microscopy (TEM) analyses

A drop of the AuNP suspension was deposited onto a carbon-coated copper grid and allowed to air-dry at room temperature. The grid was then analyzed under an accelerating voltage of 80 kV and irradiated with a uniform electron beam generated by a thermionic tungsten filament. Images were acquired at magnifications of 200,000×, 50,000×, and 20,000×. Nanoparticle diameters were measured using ImageJ® software (free version), which determines particle area. The measurement data were transferred to Microsoft Excel, where particle radius (r) and diameter (d) were calculated according to Eq 1. Nanoparticle size was expressed as the mean particle diameter.

$$A = \pi r^2; d = 2r \quad (1)$$

Dynamic Light Scattering (DLS) analyses

The hydrodynamic diameter distribution of the synthesized AuNPs–Vo was determined by dynamic light scattering (DLS) according to ISO 22412:2017 guidelines using a Nanopartica SZ-100 analyzer (Horiba Instruments, Kyoto, Japan). For analysis, 0.5 mL of the nanoparticle suspension was diluted with 1.5 mL of ultrapure water and transferred to a four-sided, optically polished polystyrene cuvette with a 1.00 cm optical path length. Light scattering measurements were performed using a 10 mW laser operating at a wavelength of 532 nm. All analyses were conducted in triplicate at 25.0 °C, with an acquisition time of 120 s and a scattering angle of 90°. The autocorrelation functions were obtained with the HORIBA NextGen Project SZ-100 software for Windows to obtain distributions of hydrodynamic diameter by Inverse Laplace transform. The cumulant method was using for calculating the polydispersity index (PI).

Zeta potential determinations

Zeta potential measurements followed the general recommendations of ISO 13099-2 for electrophoretic mobility and zeta potential determination, using the same instrument and software as the DLS analyses. Samples were prepared in aqueous medium and transferred to a 6 mm carbon electrode cell. All measurements were performed in triplicate at 25.0 °C. Zeta potential values were calculated according to the Smoluchowski model, which describes the electrokinetic behavior of particles in suspension and is widely used to assess colloidal stability. Data normality was evaluated using the Shapiro–Wilk test. Since zeta potential data did not meet normality assumptions ($p < 0.05$), comparisons between groups were performed using the Mann–Whitney test.

Surface-Enhanced Raman Scattering (SERS) analyses

Samples were prepared by the successive deposition of five drops of the colloidal suspension (20 µL per drop) onto a previously cleaned glass substrate, followed by drying at 50 °C. Surface-enhanced Raman scattering (SERS) spectra were acquired using an XploRA Raman spectrometer (HORIBA Scientific) with an excitation wavelength of 532 nm. The laser beam was focused onto the sample using a 100× objective lens, with an incident intensity of approximately 100 W mm^{-2}, a 100 µm slit, a 300 µm hole, and a 1200 gr mm^{-1} diffraction grating. The spectra were recorded over the spectral range of 500–3500 cm^{-1} using an acquisition time of 60 s and three accumulations for each measurement. To account for sample heterogeneity, multiple SERS spectra were collected from different regions of each substrate, and the final spectrum corresponded to the average of all recorded spectra.

Gold mass determinations

The determination of gold (Au) concentration was performed by inductively coupled plasma optical emission spectrometry (ICP-OES). The analyses were conducted using an ICP-OES spectrometer (Optima 7300 DV spectrometer - PerkinElmer), equipped with a electrospray glass expansion nebulizer, associated with a Scott-type chamber. Three independent syntheses were performed under optimized conditions (pH 8.3, extract concentration of 1 mg mL^{-1}, three replicated weightings per synthesis, and dilution of $HAuCl_4$ twice). For each analysis, 100 µL of the sample from each synthesis were transferred to previously labeled 15 mL Falcon tubes, followed by the addition of 100 µL of 65% HNO_3 for digestion of the material. Three blank samples, each containing 200 µL of HNO_3, were prepared in parallel. The samples were incubated for 24 h and then heated in a water bath at 100 °C for 5 h to ensure complete digestion. After digestion, 9 mL of deionized water were added to each tube, and the samples were analyzed by ICP-OES.

Gold quantification was performed using an external calibration curve, with calibration points of 0.2, 0.5, 1.0, and 2.0 mg L^{-1}, yielding a correlation coefficient of 0.999997. The analytical signal was monitored at the characteristic gold wavelength (242.795 nm), selected based on sensitivity, absence of spectral interferences, and axial view configuration. ICP-OES operating conditions were as follows: plasma gas flow of 15 L min^{-1}, auxiliary gas flow of 0.5 L min^{-1}, and nebulizer gas flow of 0.6 L min^{-1}. A SeaSpray concentric nebulizer coupled to a Twister glass cyclonic spray chamber was employed. The sample aspiration rate was set at 1.5 mL min^{-1}, and radiofrequency power was maintained at 1400 W. Analytical quality control included blank analyses, spiked samples, and precision assessment through triplicate analyses. The instrumental limit of detection (LOD) was 0.0001 mg L^{-1}. Data normality was assessed using the Shapiro–Wilk test. As ICP-OES data met normality assumptions ($p > 0.05$), statistical comparisons between groups were performed using Student's t-test.

Flocculation degree analysis

The stability of AuNPs–Vo under different conditions, including variations in temperature, ionic strength, and surface charge, was evaluated using the flocculation test, commonly referred to as the flocculation parameter [63].

Temperature stability was assessed at 20, 40, 60, and 80 °C, as well as under autoclaving conditions. For each assay, 500 µL of the AuNPs–Vo suspension were transferred to pre-labeled sterile polypropylene microtubes

To evaluate the effects of pH and ionic strength, 500 µL of solutions with varying pH values (1–13) or NaCl concentrations (1, 2.5, 5, 10, 25, 50, 100, and 200 mmol L^{-1}) were added to the nanoparticle suspensions. Acidic and basic conditions were achieved using 0.1 mol L^{-1} HCl or NaOH, and pH values were verified using a calibrated pH meter. For temperature and autoclave experiments, 500 µL of ultrapure water were added instead of salt or pH-adjusted solutions.

After incubation for 1 h, the resulting suspensions were analyzed in triplicate by UV–Vis spectroscopy at 600 nm. The absorbance at this wavelength, expressed as the area under the curve (AUC), was used as an indicator of nanoparticle aggregation and colloidal stability (Equation S3). Higher AUC values correspond to increased particle aggregation and, consequently, reduced nanoparticle stability.

Cytotoxicity assays

Vero cells were cultured in Dulbecco's Modified Eagle Medium (DMEM) supplemented with 10% fetal bovine serum, 1% L-glutamine, and a penicillin/streptomycin solution (ThermoFisher) and maintained at 37 °C in a humidified incubator with 5% CO_2. Prior to treatment, culture medium sterility was verified, and cell numbers were determined using a Neubauer hemocytometer with Trypan Blue exclusion. Based on the cell count, 1×10^6 cells were seeded in 60 mm culture plates and incubated for 24 h to allow cell attachment.

Cells were then treated with 100 µL of $HAuCl_4$ solution (2.5×10^{-4} mol L^{-1}), aqueous extract (1 mg mL^{-1}), or AuNPs–Vo at 100%, 60%, and 20% concentrations, and incubated for either 24 or 96 h (Table 1). Following incubation, the cells were washed with phosphate-buffered saline (PBS), detached, collected into microtubes, and stored at −30 °C for subsequent analyses, including oxidative stress biomarker assays. Ultrapure water was used as the negative control. Cell viability was assessed using the MTT assay. Briefly, Vero cells (1×10^6 cells mL^{-1}) were seeded into 96-well plates and allowed to adhere for 24 h prior to treatment. Cells were then exposed to 50 µL of aqueous extract, AuNPs–Vo, or $HAuCl_4$ at 100%, 60%, and 20% concentrations. Wells containing culture medium supplemented with 50 µL of ultrapure water were used as the negative control. After incubation periods of 24 h and 96 h, cell viability was evaluated by adding MTT reagent followed by incubation for 4 h. The resulting formazan crystals were solubilized with 80 µL of 10% dimethyl sulfoxide (DMSO), and absorbance was measured at 595 nm. Formazan formation, indicated by a blue-violet coloration, reflects mitochondrial metabolic activity and serves as an indicator of cell viability. Higher absorbance values correspond to increased numbers of viable cells and lower cytotoxic effects. Viability index was calculated as a ratio based on untreated cells, that were considered as 100% viability.

Table 1 Concentration ratios of the materials [value (legend)] cells were exposed to in the cytotoxicity assays

	AuNPs	Extract	$HAuCl_4$
100 %	50.01 mg mL^{-1} (N100) *	1.0 mg mL^{-1} (E100)	$2.5x10^{-4}$ mol L^{-1} (O100)
60 %	30.00 mg mL^{-1} (N60)	0.6 mg mL^{-1} (E60)	$1.5x10^{-4}$ mol L^{-1} (O60)
20 %	10.00 mg mL^{-1} (N20)	0.2 mg mL^{-1} (E20)	$0.5x10^{-4}$ mol L^{-1} (O20)

The table was organized using Microsoft Excel 2016 (Microsoft Corporation, Redmond, WA, USA).

Estimated value obtained by summing the mass of elemental Au and the mass of extract that reacted to form the AuNPs–Vo.

Oxidative stress assessments

Cells exposed to AuNPs–Vo, aqueous extract, or $HAuCl_4$ were lysed by vortexing for 30 s and subsequently centrifuged at 1,500 rpm for 5 min to separate the protein-containing supernatant from cellular debris. The pellets were discarded, and the supernatants were transferred to new Eppendorf microtubes and stored at −30 °C until further analyses. Total protein content was determined in triplicate using a modified Lowry method [68], with absorbances determined at 750 nm and bovine serum albumin (BSA) used as the standard. Samples and BSA standards were mixed with a light-sensitive reagent A containing Na_2CO_3, $KNaC_4H_4O_6$, $CuSO_4$, NaOH, and SDS, followed by incubation with the Folin–Ciocalteau reagent in the dark for 30 min. Absorbance readings were obtained in triplicate using 96-well plates, and protein concentrations were calculated from the corresponding standard curve. These values were subsequently used to normalize measurements of oxidative stress biomarkers and enzymatic activities.

Reduced glutathione (GSH) and glutathione S-transferase (GST) determinations

Cellular reduced glutathione (GSH) levels were determined according to Wilhelm Filho et al. [87], with absorbances determined at 412 nm using GSH as the standard. A seven-point calibration curve was prepared using GSH (10 mmol L^{-1}) dissolved in 0.1 mol L^{-1} sodium phosphate buffer (pH 7.0), with ultrapure water serving as the blank. Samples were diluted threefold in ultrapure water, mixed with 350 µL of DTNB reagent, and incubated for 15 min. Absorbance

readings were obtained in triplicate using a UV–Vis spectrophotometer (UV-M51, Bel).

Cellular glutathione S-transferase (GST) activity was determined according to the method described by Habig, Pabst and Jakoby [48]. Cells were homogenized in 0.1 mol L^{-1} sodium phosphate buffer (pH 6.5) containing 0.25 mmol L^{-1} sucrose and 1 mmol L^{-1} EDTA, followed by centrifugation at 11,000 × g for 30 min at 4 °C. The resulting supernatants were diluted in buffer, and GST activity was measured spectrophotometrically at 340 nm over a 60 s interval [48].

Hydrogen peroxide (H_2O_2) and Catalase (CAT) determinations

Cellular hydrogen peroxide (H_2O_2) levels were quantified according to Alexieva et al. [4], with absorbances measured at 390 nm using a UV–Vis spectrophotometer (UV-M51, Bel). Hydrogen peroxide was used as the external standard. A 10-point calibration curve was prepared using H_2O_2 diluted in 0.1% (m/v) trichloroacetic acid (TCA), with ultrapure water serving as the blank. For the assay, 125 µL of each standard or sample was transferred to sterile 2 mL polypropylene tubes and mixed with 125 µL of 100 mM potassium phosphate buffer (pH 7.5) and 250 µL of 1 M potassium iodide (KI). The mixtures were incubated on ice in the dark for 1 h, after which absorbances were determined in triplicate at 390 nm on a UV–Vis spectrophotometer.

Catalase (CAT) activity was determined using hydrogen peroxide (H_2O_2) as the substrate and ammonium molybdate to terminate the reaction, according to the Goth method [46]. All reagents were prepared in 0.06 mol L^{-1} sodium phosphate buffer (pH 7.4). For each sample, two Eppendorf tubes were prepared: Tube 1 (reaction tube), containing 500 µL of buffer and 100 µL of sample, and Tube 2 (reference tube), containing 500 µL of ammonium molybdate, 500 µL of buffer, and 100 µL of sample. Both tubes were incubated at 35 °C for 1 min. Subsequently, 500 µL of H_2O_2 was added to Tube 1, followed by incubation for an additional 1 min. The reaction was then stopped by adding ammonium molybdate. Absorbances were measured in triplicate at 405 nm using a UV–Vis spectrophotometer, and CAT activity was calculated based on the difference in absorbance between the reaction and reference tubes [46].

Lipid Peroxidation (MDA) and carbonylated protein (PTC) determinations

Lipid peroxidation in tissues and serum was evaluated using a modified Cayman Chemical thiobarbituric acid reactive substances (TBARS) assay, with malondialdehyde (MDA) employed as the standard. A calibration curve was constructed using 11 MDA concentrations ranging from 10 to 700 µL diluted in ultrapure water. Samples were prepared by diluting 20 µL of each sample in 980 µL of ultrapure water. For the assay, 150 µL of each diluted sample or standard was mixed with 150 µL of 10% trichloroacetic acid and 1,200 µL of thiobarbituric acid solution prepared in acetic acid containing 20% NaOH. The reaction mixtures were heated at 85 °C for 1 h and subsequently cooled on ice for 10 min. Absorbance readings were obtained in triplicate at 532 nm using 96-well plates. The formation of a pink MDA–TBA adduct is directly proportional to the MDA concentration, which was quantified by interpolation from the standard curve [32].

Protein carbonyl content was determined in 96-well plates. For blank measurements, 80 µL of each sample was mixed with 80 µL of 0.5 mol L^{-1} H_3PO_4, whereas for carbonyl determination, 80 µL of sample was reacted with 80 µL of 2,4-dinitrophenylhydrazine (DNPH). After incubation for 10 min in the dark, 40 µL of 6 mol L^{-1} NaOH was added to each well. Absorbances were determined in triplicate at 450 nm using a UV–Vis spectrophotometer (UV-M51, Bel) [61].

Total antioxidant Capacity (CAOT)

The antioxidant activity of AuNPs–Vo and the corresponding aqueous extract was evaluated according to International Organization for Standardization (2009) [51] with modifications. Briefly, $ABTS^{\bullet+}$ radical cation was generated by reacting ABTS with potassium persulfate and allowing the mixture to incubate for 16 h at 4 °C. The resulting radical solution was diluted in ethanol and adjusted to an absorbance of 0.70 ± 0.02 at 734 nm. Samples and Trolox® standards were incubated with the $ABTS^{\bullet+}$ solution for 6 min, and absorbance readings were obtained in triplicate at 734 nm.

Statistical analyses

The UV–Vis absorbance data were processed using OriginPro® 2024 (trial version). Significant variables identified from the full factorial design were analyzed using Statistica® 8.0 (trial version) through analysis of variance (ANOVA), with effects evaluated using Pareto diagrams. The normality of all datasets was assessed using the Shapiro–Wilk test to determine the suitability of parametric or non-parametric statistical analyses. For datasets displaying a normal distribution, ANOVA was followed by Tukey's post hoc test for multiple comparisons or Dunnett's test when comparisons were made against a control group; for datasets showing non-normal distribution, ANOVA was followed by Kruskal Wallis and Dunn's test when comparisons were made against a control group. Only Spearman's

correlation was applied, as the analysis aimed to evaluate the influence of one biomarker on another, and all biomarkers, except catalase, showed non-normal distributions. All statistical analyses were performed at a significance level of $p \leq 0.05$. The Limits of Detection (LOD) and Limits of Quantification (LOQ), when applicable, were estimated based on the slope of the calibration curve and the standard deviation of the blank, using multiplicative factors of 3 and 10, respectively.

A Principal Component Analysis (PCA) was performed using data obtained from antioxidant system, oxidative stress, and cytotoxicity assessments. For PCA, the strength of associations among variables was estimated using Spearman correlation coefficients, according to data distribution, following the criteria proposed by Fávero [34]. The suitability of the dataset for PCA was verified using the Kaiser–Meyer–Olkin (KMO) index (Figure S4).

The Integrated Biomarker Response version 2 (IBRv2) was calculated to integrate multiple biochemical biomarkers into a single index of biological disturbance, following the approach proposed by Sanchez et al. [76] with adaptations to preserve the toxicological interpretation of biomarker responses.

For each biomarker, the mean value obtained for each treatment group was standardized relative to the control group (Equation S4). To preserve biological interpretation, signs were assigned according to the expected toxicological meaning of each biomarker. For biomarkers in which an increase is generally associated with adverse effects (e.g., lipid peroxidation, protein carbonylation, hydrogen peroxide), positive deviations were maintained, while decreases received negative values. Conversely, for biomarkers associated with antioxidant defense or cellular protection (CAT, GST, GSH, MTT), decreases relative to control were considered adverse and therefore assigned negative values, whereas increases were maintained as positive values.

After sign attribution, biomarker scores were plotted in radar charts to visualize the response profile of each treatment group relative to control. To estimate the global magnitude of biological disturbance and avoid cancellation between antagonistic biomarker responses, the final IBRv2 score for each treatment was calculated as the sum of the absolute standardized values (Equation S5). Higher IBRv2 values indicate greater overall biological disturbance relative to the control group. Graphical representations of the results were generated using GraphPad Prism® version 8.4. Additional software used for data analysis included Microsoft Excel, R Studio®, OriginPro®, Statistica®, and ImageJ®.

Results and discussion

Virola oleifera AuNPs synthesis

All synthesized nanoparticles produced solutions with a characteristic reddish coloration and maximum values of localized surface plasmon resonance (LSPR) bands (λ_max) in the 500–600 nm range. This observation is consistent with reports by Keijok et al. [56] and Silva et al [79], who indicate that AuNPs exhibit a ruby-red color due to the excitation of surface plasmon vibrations, generating the LSPR band centered around 536 nm [49]. The LSPR band shifts to higher wavelengths with increasing nanoparticle concentration and surface exposure time, reflecting the formation of more or larger AuNPs with sizes corresponding to λ_max values between 536 and 544 nm [66]. For noble metal nanoparticles, particularly gold and silver, the LSPR occurs in the visible region, and its intensity and wavelength depend on factors affecting electron density at the nanoparticle surface, such as metal type, size, shape, structure, composition, and the dielectric constant of the medium [26].

Both the maximum optical density (Abs_max) and full width at half maximum (FWHM) of the LSPR bands were influenced by particle shape. The observed reddish color and λ_max between 500–600 nm indicate that the synthesized AuNPs–Vo are spherical [13]. Smaller spherical AuNPs yield λ_max values closer to 500 nm, producing a bright red color, while larger spherical AuNPs show λ_max near 600 nm, resulting in a purple hue [10, 20, 26, 30, 44]. Previous studies have shown that spherical AuNPs exhibit LSPR bands between 500–600 nm, with values in this range reflecting size distribution and stability. For example, Balasubramanian et al. [10], reported a well-defined LSPR peak at 547 nm, indicating homogeneous AuNPs, while λ_max between 525–555 nm corresponded to ultrafine nanoparticles. Fayaz et al. [35] associated strong LSPR signals at ~423 nm with stable AuNPs, observing increased absorbance after 24 h, highlighting the influence of reaction time on particle stability. Similarly, Sharma et al. [77] monitored UV–Vis spectra for reactions with varying $HAuCl_4$ concentrations over time, noting that AuNP formation was primarily indicated by the color change from yellow to wine red within 40 minutes after addition of *C. japonica* leaf extract.

A total of 32 samples were evaluated using a full factorial design (2^5), where 2 corresponds to the lower and upper levels of each factor, and 5 represents the number of variables (Table 2). Pareto diagrams allow visualization and identification of variables that significantly influenced the synthesis of AuNPs–Vo (Figure S1 and S2). Regarding yield or higher nanoparticle concentrations, represented by maximum optical density (Abs.max), Figure S1a and S2a indicates that time (1) and the linear interaction between extract concentration

Table 2 Results of the full factorial design for AuNPs [values (standard deviation)], including the variables time (t), temperature (T), extract concentration, pH, and agitation, along with their respective response variables: maximum LSPR band wavelength (λ.max), maximum optical density (Abs_max), full width at half maximum (FWHM), and area under the curve (AUC)

N	t (min)	T (°C)	Extract (mg mL^{-1})	pH	Shaking (rpm)	λ (max)	Abs (max)	FWHM	AUC
1	6 (-)	25 (-)	0.5 (-)	4.3 (-)	200 (-)	557 (19.7)	0.005 (0)	72 (14.42)	0.044 (0.03)
2	6 (-)	25 (-)	0.5 (-)	4.3 (-)	400 (+)	528 (0)	0.009 (0.01)	71.33 (16.4)	0.06 (0.02)
3	6 (-)	25 (-)	0.5 (-)	8.3 (+)	200 (-)	532 (3.46)	0.011 (0.01)	68 (2.65)	0.001 (0.01)
4	6 (-)	25 (-)	0.5 (-)	8.3 (+)	400 (+)	523.67 (17.04)	0.006 (0.01)	74.33 (8.39)	0.053 (0.03)
5	6 (-)	25 (-)	1.5 (+)	4.3 (-)	200 (-)	527 (0)	0.008 (0)	38 (3)	0.007 (0.03)
6	6 (-)	25 (-)	1.5 (+)	4.3 (-)	400 (+)	524 (1)	0.003 (0)	3.667 (5.13)	0.044 (0.01)
7	6 (-)	25 (-)	1.5 (+)	8.3 (+)	200 (-)	516.33 (2.52)	0.032 (0.05)	53.667 (9.5)	0.044 (0.04)
8	6 (-)	25 (-)	1.5 (+)	8.3 (+)	400 (+)	517.33 (2.08)	0 (0)	0 (0)	0.044 (0)
9	6 (-)	40 (+)	0.5 (-)	4.3 (-)	200 (-)	523.33 (2.31)	0.006 (0)	37 (10.44)	0.064 (0.05)
10	6 (-)	40 (+)	0.5 (-)	4.3 (-)	400 (+)	527.67 (2.08)	0.021 (0.02)	56.67 (4.79)	0.064 (0.02)
11	6 (-)	40 (+)	0.5 (-)	8.3 (+)	200 (-)	529 (4.04)	0.065 (0.01)	72.33 (7.43)	0.044 (0.15)
12	6 (-)	40 (+)	0.5 (-)	8.3 (+)	400 (+)	534.67 (0)	0.039 (0.01)	92 (20.21)	0.001 (0.03)
13	6 (-)	40 (+)	1.5 (+)	4.3 (-)	200 (-)	534.67 (0.58)	0.019 (0.01)	57.67 (1.53)	0.058 (0.03)
14	6 (-)	40 (+)	1.5 (+)	4.3 (-)	400 (+)	534.67 (2.65)	0.01 (0.01)	53.33 (9.46)	0.123 (0.19)
15	6 (-)	40 (+)	1.5 (+)	8.3 (+)	200 (-)	530 (10.39)	0 (0)	0 (0)	0.107 (0)
16	6 (-)	40 (+)	1.5 (+)	8.3 (+)	400 (+)	512 (17.9)	0 (0.01)	0 (46.77)	0.092 (0.16)
17	11 (+)	25 (-)	0.5 (-)	4.3 (-)	200 (-)	542 (2.65)	0.017 (0)	89.67 (1.53)	0.12 (0.02)
18	11 (+)	25 (-)	0.5 (-)	4.3 (-)	400 (+)	537 (2)	0.017 (0.01)	72 (0.58)	0.099 (0.07)
19	11 (+)	25 (-)	0.5 (-)	8.3 (+)	200 (-)	540.33 (0.58)	0.025 (0)	71.33 (3.46)	0.069 (0.03)
20	11 (+)	25 (-)	0.5 (-)	8.3 (+)	400 (+)	538 (1.53)	0.015 (0)	58.67 (1.53)	0.003 (0.02)
21	11 (+)	25 (-)	1.5 (+)	4.3 (-)	200 (-)	537 (0.58)	0.013 (0)	53.33 (2.31)	0.06 (0.01)
22	11 (+)	25 (-)	1.5 (+)	4.3 (-)	400 (+)	534.67 (1.73)	0.009 (0.01)	50.67 (4.04)	0 (0)
23	11 (+)	25 (-)	1.5 (+)	8.3 (+)	200 (-)	527.33 (0)	0.01 (0)	48.33 (25.4)	0 (0.2)
24	11 (+)	25 (-)	1.5 (+)	8.3 (+)	400 (+)	522 (1.53)	0 (0)	0 (0)	0 (0)
25	11 (+)	40 (+)	0.5 (-)	4.3 (-)	200 (-)	519 (7.51)	0 (0.01)	0 (42.15)	0.108 (0.27)
26	11 (+)	40 (+)	0.5 (-)	4.3 (-)	400 (+)	532 (0)	0.013 (0.03)	75 (12.12)	0.17 (0.01)
27	11 (+)	40 (+)	0.5 (-)	8.3 (+)	200 (-)	532 (0.58)	0.057 (0.01)	92.333 (1)	0.064 (0.04)
28	11 (+)	40 (+)	0.5 (-)	8.3 (+)	400 (+)	531.67 (0.58)	0.037 (0.01)	86.33 (19.4)	0.057 (0.03)
29	11 (+)	40 (+)	1.5 (+)	4.3 (-)	200 (-)	532 (0.58)	0.017 (0.01)	51 (4.93)	0.062 (0.06)
30	11 (+)	40 (+)	1.5 (+)	4.3 (-)	400 (+)	530.67 (1.73)	0.012 (0)	46 (0)	0.1 (0)
31	11 (+)	40 (+)	1.5 (+)	8.3 (+)	200 (-)	519 (10.61)	0 (0.13)	0 (69.3)	0.044 (0.56)
32	11 (+)	40 (+)	1.5 (+)	8.3 (+)	400 (+)	519 (10.61)	0 (0.13)	0 (69.3)	0.044 (0.56)

Representation of the upper limit (+) and lower limit (-). The table was organized using Microsoft Excel 2016 (Microsoft Corporation, Redmond, WA, USA)

([extract], 3) and pH (4) were the most significant factors. Similar results were observed for the area under the curve (AUC) analysis (Figure S1d and S2d). For FWHM (Figure S1b and S2b) and λ.max (Figure S1c and S2c), the variables [extract] (3), pH (4), and their linear interaction (3 × 4) were responsible for producing spherical AuNPs–Vo with lower aggregation and reduced polydispersity.

An ANOVA analysis indicated that, with 95% confidence, the statistically significant variables were pH, reaction time, and extract concentration, which were consequently selected for the optimized factorial design experiments (Table 3). The remaining variables were considered negligible, as their calculated effects could be disregarded with 95% confidence. Similar findings were reported by Contreras et al [26] and Marques (2020), who identified pH and time as significant factors in their optimized factorial designs. The significance of these variables can be attributed to the antioxidant molecules present in the extract, which exhibit high protonation and deprotonation potential, as well as to the charged nature of AuNPs. Changes in pH can alter these characteristics, leading to particle aggregation or electrostatic repulsion. Similarly, extract concentration and reaction time can influence both particle aggregation/repulsion and the overall yield of AuNPs–Vo.

Previous studies have shown that reaction time is crucial for obtaining stable, monodisperse AuNPs, as discussed by Fayaz et al. [35], who observed stability after 24 hours of reaction between the gold salt and the plant extract. Initially, nanoparticle morphology was highly variable, with predominantly spherical particles and occasional rod-like forms

Table 3 Response matrix of the 27 syntheses [values (standard deviation)], performed in the optimized factorial design to evaluate the best synthesis condition for AuNPs-Vo, considering the significant variables: reaction time (t), extract concentration ([_]), and pH, as well as the corresponding response variables: maximum LSPR band wavelength (λ,max), maximum optical density (Abs. max), full width at half maximum (FWHM), and area under the curve (AUC)

N	[Extract] (mg mL^{-1})	t (min)	pH	λ (max)	Abs (max)	FWHM	AUC
1	4,3 (-)	0,5 (-)	6 (-)	537 (2,9)	0,118 (0,03)	95 (1,25)	0,422 (0,01)
2	4,3 (-)	0,5 (-)	9 (0)	539 (0,49)	0,189 (0,02)	90 (4,38)	0,381 (0,04)
3	4,3 (-)	0,5 (-)	11 (+)	532 (2,55)	0,15 (0,03)	99 (4,99)	0,352 (0,03)
4	4,3 (-)	1,0 (0)	6 (-)	539 (0,6)	0,08 (0,01)	104 (1,04)	0,422 (0,03)
5	4,3 (-)	1,0 (0)	9 (0)	538 (2,44)	0,181 (0,01)	100 (0,22)	0,354 (0,02)
6	4,3 (-)	1,0 (0)	11 (+)	539 (2,89)	0,14 (0,0)	101 (4,52)	0,385 (0,03)
7	4,3 (-)	1,5 (+)	6 (-)	547 (2,96)	0,168 (0,02)	108 (2,08)	0,47 (0,0)
8	4,3 (-)	1,5 (+)	9 (0)	542 (3,32)	0,128 (0,0)	88 (3,74)	0,42 (0,02)
9	4,3 (-)	1,5 (+)	11 (+)	541 (0,99)	0,115 (0,02)	88 (3,84)	0,406 (0,03)
10	6,3 (0)	0,5 (-)	6 (-)	529 (2,09)	0,028 (0,01)	108 (1,18)	0,449 (0,04)
11	6,3 (0)	0,5 (-)	9 (0)	535 (0,79)	0,096 (0,01)	98 (0,5)	0,403 (0,04)
12	6,3 (0)	0,5 (-)	11 (+)	541 (0,23)	0,151 (0,02)	87 (5,11)	0,411 (0,0)
13	6,3 (0)	1,0 (0)	6 (-)	514 (2,58)	0,266 (0,03)	87 (2,88)	0,358 (0,01)
14	6,3 (0)	1,0 (0)	9 (0)	552 (1,29)	0,142 (0,0)	107 (1,64)	0,444 (0,03)
15	6,3 (0)	1,0 (0)	11 (+)	550 (3,17)	0,056 (0,0)	126 (0,11)	0,53 (0,0)
16	6,3 (0)	1,5 (+)	6 (-)	551 (0,92)	0,037 (0,02)	98 (2,95)	0,395 (0,02)
17	6,3 (0)	1,5 (+)	9 (0)	544 (1,27)	0,127 (0,02)	72 (1,0)	0,401 (0,04)
18	6,3 (0)	1,5 (+)	11 (+)	547 (2,87)	0,171 (0,01)	101 (4,62)	0,406 (0,01)
19	8,3 (+)	0,5 (-)	6 (-)	551 (1,87)	0,17 (0,01)	50 (2,89)	0,416 (0,02)
20	8,3 (+)	0,5 (-)	9 (0)	550 (2,82)	0,204 (0,03)	71 (2,82)	0,42 (0,02)
21	8,3 (+)	0,5 (-)	11 (+)	532 (2,77)	0,076 (0,01)	34 (5,55)	0,476 (0,02)
22	**8,3 (+)**	**1,0 (0)**	**6 (-)**	**535 (0,4)**	**0,204 (0,02)**	**38 (2,66)**	**0,327 (0,03)**
23	8,3 (+)	1,0 (0)	9 (0)	547 (0,88)	0,139 (0,01)	34 (3,32)	0,285 (0,02)
24	8,3 (+)	1,0 (0)	11 (+)	535 (3,49)	0,174 (0,0)	92 (4,05)	0,376 (0,04)
25	8,3 (+)	1,5 (+)	6 (-)	531 (2,19)	0,13 (0,02)	80 (0,14)	0,436 (0,03)
26	8,3 (+)	1,5 (+)	9 (0)	532 (2,59)	0,142 (0,0)	82 (3,51)	0,423 (0,03)
27	8,3 (+)	1,5 (+)	11 (+)	532 (2,72)	0,128 (0,01)	84 (2,53)	0,411 (0,04)

The optimal condition is highlighted in bold (condition 22). Representation of the upper limit (+), lower limit (-), and central limit (0). The table was organized using Microsoft Excel 2016 (Microsoft Corporation, Redmond, WA, USA).

ranging from 5 to 40 nm in diameter. Over time, up to 24 hours, the nanoparticles stabilized; however, they remained polydisperse, likely due to the lack of pH control. These authors concluded that optimizing experimental conditions, including pH, temperature, and metal ion concentration, is essential for producing uniformly shaped nanoparticles. Similarly, Chahardoli et al. [20] observed nearly spherical AuNPs but did not achieve monodispersity, reporting the presence of larger nanoparticles with triangular, pentagonal, and hexagonal shapes. In Contreras et al. [26], the applied experimental design allowed the identification of experimental factors that influence the physicochemical properties of gold nanoparticles (AuNPs), directly affecting their size and, consequently, their dispersion, where pH variation directly influences Δλ and, consequently, the variation in the size of the AuNPs. Similarly, the AuNPs of Marques, (2020), under controlled synthesis conditions were monodisperse, with an average size of 22 nm and quasi-spherical according to the TEM image. These results further highlight the critical importance of controlling synthesis conditions to obtain uniform and stable AuNPs.

Virola oleifera aqueous extract characterizations

Liquid Chromatography coupled to UV detection analysis

To evaluate the chromatographic profile of the extract and identify compounds involved in gold nanoparticle formation, HPLC analyses were performed on the solvent, extract, and post-synthesis supernatant. Figure S3a presents the chromatogram of the blank, consisting of ultrapure water, which was used as the dissolving solvent. Figures S3b and S3c correspond to the aqueous extract and the supernatant obtained after AuNPs–Vo synthesis, respectively. Comparison of the three chromatograms reveals the presence of compounds originating from both the plant extract and the solvent. Peaks 1 to 16 observed in Figure S3b, with retention times between 5 and 15 min, correspond to compounds exclusive to the extract. In Figure S3c, these peaks exhibit

reduced intensities, indicating lower concentrations of these molecules and suggesting that a substantial fraction reacted partially or completely with gold ions during the synthesis of AuNPs–Vo.

The shape of the peaks is narrow and uniform, indicating that each corresponds to a specific molecule or a group of structurally similar molecules. Peaks in close proximity may share similar functional groups or chemical characteristics. Peak 17 is increased in Figure S3b and decrease in Figure S3c, indicating that the compounds represented by this peak also participated in the gold reduction process. Unlike the other peaks, peak 17 is broader and less homogeneous, suggesting more than one molecular species is detected in this region. To further investigate the composition of *V. oleifera* extract an HPLC-MS was performed.

Ultra-high-performance liquid chromatography coupled to mass spectrometry (UHPLC–MS)

In ultra-high-performance liquid chromatography coupled to mass spectrometry (UHPLC–MS), the method required adaptation because trifluoroacetic acid is not compatible with mass spectrometric detection and was therefore replaced with formic acid. In addition, the mobile phase gradient had to be adjusted, and the column was replaced to accommodate UHPLC rather than conventional HPLC conditions. Figure 1A shows the chromatogram obtained using the adapted method, which is very similar to that of the HPLC method but with a shorter run time, as expected. However, evaluation of the mass chromatogram (Fig. 1B) revealed that only minor compounds were ionized, with major peak ionization not achieved.

Notation of the ionized compounds was performed by molecular networking. Only a limited number of molecular networks were generated, suggesting low chemical complexity of the extract. Library research indicated the presence of procyanidin B1 and procyanidin C1 (Fig. 2A). The network containing the nodes corresponding to these compounds (Fig. 2B) was examined using mirrored spectra, fragmentation pathways, and comparison with literature data [74]. Procyanidin B1 was detected in the network as both a protonated ion ($[M+H]^+$, m/z 579) and a deprotonated ion ($[M-H]^-$, m/z 577), exhibiting equivalent fragmentation pathways for both ionization modes (Fig. 2C and D). Procyanidin C1 was also observed as protonated and deprotonated ions (m/z 867 and m/z 865, respectively), and its structure and fragments were consistent with the proposed fragmentation pathways (Fig. 2E). The node at m/z 1155.2800 was consistent with a $[M-H]^-$ adduct of a procyanidin B–type dimer (Rue; Rush; Van Breemen, 2018). These findings

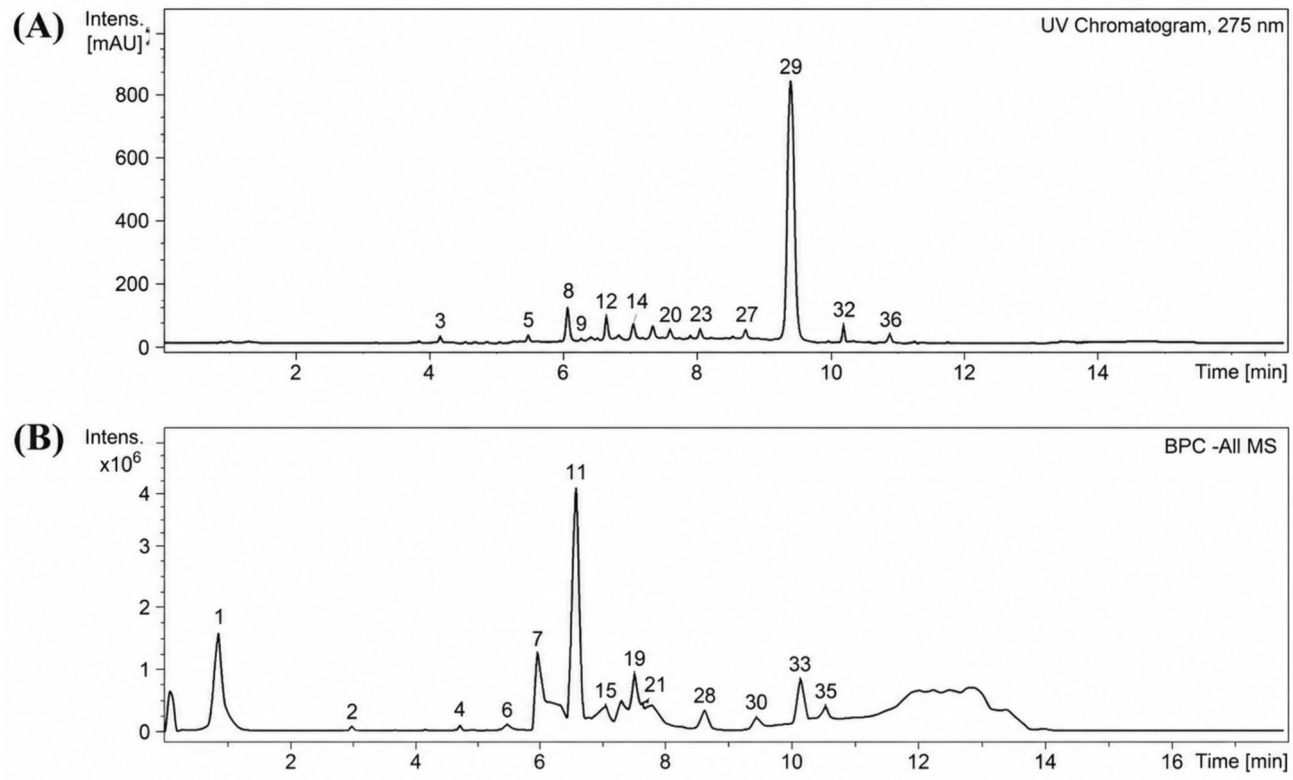


Fig. 1 Aqueous *Virola oleifera* extract of analyzed by UHPLC (**A**) and UHPLC–MS (**B**) using ProteoWizard (MSConvert v. 3.0.24338) and subsequently processed in MZmine (v. 2.53)

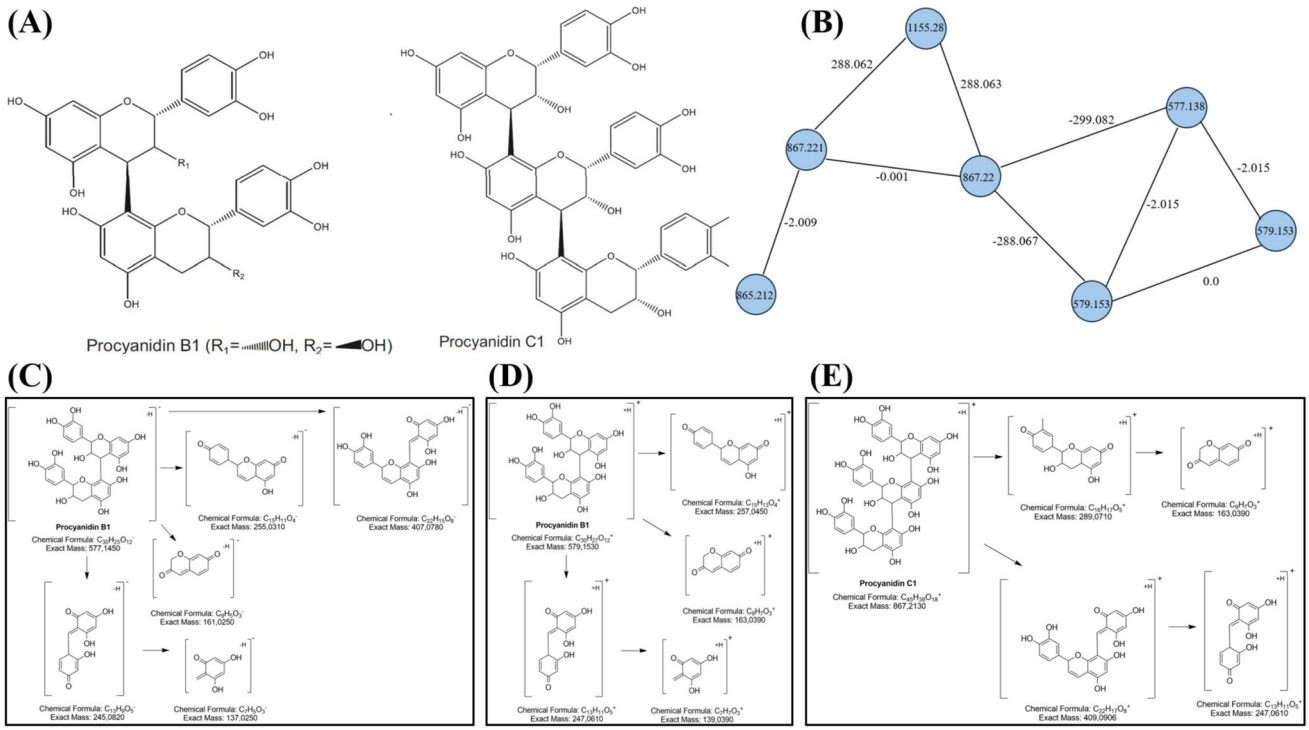


Fig. 2 Procyanidins B1 and C1 molecular structures (**A**) (Adapted from [74]), molecular network generated through HPLC-ESI-MS/MS data of the aqueous extract of *V. oleifera* (**B**), fragmentation pathway for Procyanidin B1 [M+H]- adduct (**C**), Fragmentation pathway for Procyanidin B1 [M+H]+ adduct (**D**) and fragmentation pathway for Procyanidin C1 [M+H]+ adduct (**E**). The resulting network was downloaded and visualized using Cytoscape (v. 3.10.2)

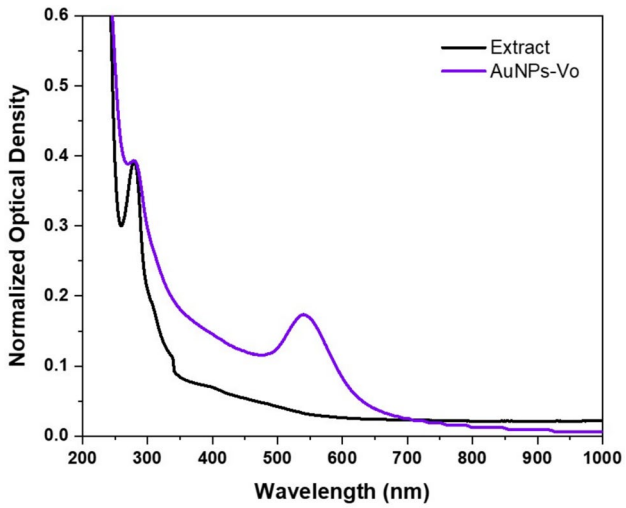


Fig. 3 UV–Vis absorption spectra of the plant extract (black line) and AuNPs-Vo (purple line), recorded in the 200–1000 nm range. The extract exhibits intense bands in the ultraviolet region (200–350 nm), attributed to phenolic compounds and other secondary metabolites. For AuNPs-Vo, a characteristic band is observed in the visible region, centered at approximately 540–560 nm, corresponding to the localized surface plasmon resonance (LSPR) of the gold nanoparticles. Spectral data processing and graph construction were performed using OriginPro 8.5 software (OriginLab Corporation, Northampton, MA, USA)

indicate the employed *V. oleifera* extract contains a significant number of phenolic compounds.

Virola oleifera AuNP characterization

UV-VIS Spectroscopy

Visible spectroscopy is one of the main techniques used to characterize AuNPs due to its high sensitivity to morphological differences, interparticle interactions, and the refractive index of the medium [19]. A total of 27 samples were analyzed according to a 3^3 experimental matrix, where the number 3 represents the three levels, namely lower (–), central (0), and upper (+), and the exponent 3 corresponds to the significant variables: pH, reaction time, and extract concentration. The synthesis condition carried out for 6 minutes, at pH 8.3, and with an aqueous extract concentration of 1.0 mg mL^{-1}, provided the best synthesis performance, being considered the optimal condition (Figure S4). The UV-VIS spectroscopy image also indicates a clear peak between 250 and 300 nm, corresponding to characteristic extract molecules. According to the spectra comparison, this peak disappears, corresponding to the AuNPs-Vo, suggesting that these molecules reacted with $HAuCl_4$ to form the AuNPs-Vo themselves (Fig. 3). In the best optimized synthesis, a numerical value of 1.71 was found by calculating

the difference between the absorbance of the extract solution at 1 mg mL^{-1} (2.25) and the supernatant from the AuNPs-Vo washes (0.53). This suggests that about 76.3% of the compounds present in the extract reacted with the gold in the synthesis, corresponding to 0.763 mg applying the curve equation.

The results suggest that plant resin contains non-reactive compounds, such as impurities, which may be present even after double filtration during collection and preparation of the pre-synthesis aqueous extract and autoclaving. These compounds, which may correspond t oinorganic salts (phosphates, sulfates and chlorides) with osmotic functions [67], in addition to polysaccharides and other structural constituents, such as sugars and vegetable gums, whose function is structural, mechanical protection and water retention [59] that do not contribute significantly to the neutralization of reactive species, are excluded in successive washes, leading to the conclusion that the washing process is indispensable.

This condition showed lower FWHM values, indicating monodisperse and less aggregated (more stable) nanoparticles, and a higher optical density (Abs_max), which reflects a greater concentration of nanomaterial in solution, *i.e.*, a higher synthesis yield. Regarding λ_max, the obtained AuNPs-Vo presented values within the typical range reported in the literature for nanoparticles smaller than 100 nm, with unique LSPR bands near 500 nm, a typical characteristic of spherical nanoparticles (Table 3). Similar results were reported by Contreras et al [26] and Marques [60], who also obtained optimal syntheses at 6 minutes of reaction and pH 7.7 (with the natural pH of the extract being 4.3). These findings suggest that the synthesis of AuNPs-Vo is practical and reproducible, as the significant variables remain consistent even when the resin is collected at different times. However, it is important to highlight that a factorial design should be performed for each new extract batch, since both the natural pH and the molecular composition of the extract can vary significantly, influencing the synthesis yield and the morphological properties of the resulting nanoparticles. The results indicate that AuNPs are best synthesized at neutral to slightly basic pH values (7–9), likely related to the molecular charges on their surfaces derived from the extract. These charges suggest a negative surface potential, as the nanoparticles interact readily with Au^{3+} ions, which are positively charged. Studies suggest that nanoparticle monodispersity is enhanced under alkaline conditions because the biomolecules acting as reducing agents in the extract adsorb negatively onto the nanoparticle surfaces [1] . [42] discuss that these negative charges, in the presence of increased OH^- concentrations, maximize electrostatic repulsion, preventing aggregation. Abdul Khalil et al. [1] also note that the short reaction time between Au^{3+} and the aqueous extract can be attributed to the highly reactive biomolecules, which contain alcoholic and carbonyl groups. pH variations influence the protonation of organic COOH groups at acidic pH and their deprotonation (COO^-) at basic pH. The deprotonated COO^- groups interact more strongly with gold atoms, stabilizing nuclei faster and preventing growth or coalescence with other smaller nuclei [42]. In contrast, at acidic pH, protonated carboxylic acids interact in a weaker manner with metal surfaces, favoring nanoparticle growth.

In the best synthesis obtained from the optimization, a numerical value of 1.71 was calculated by subtracting the absorbance of the extract solution at 1 mg mL^{-1} (2.25) from the supernatant of the AuNPs-Vo washes (0.53). This suggests that approximately 76.3% of the compounds present in the extract reacted with gold during the synthesis, corresponding to 0.763 mg according to the standard curve. The resulting percentage indicates that the *V. oleifera* resin contains non-reactive compounds, such as impurities, which may remain despite double filtration (during collection and extract preparation before synthesis) and autoclaving. These compounds are removed during successive washing steps, highlighting the necessity of this procedure. The fraction of compounds that reacted can be attributed to highly reactive molecules, such as phenolic compounds, terpenes, tannins, and vitamins. This high percentage is promising for producing nanomaterials with surfaces enriched in antioxidant agents, providing various protective effects as discussed in this study. These findings are further supported by the HPLC-UV and HPLC-MS analyses.

Transmission Electron Microscopy (TEM)

The TEM images displayed in Fig. 4 (A, B, and C) corroborate with the LSPR bands, revealing spherical nanoparticles with diameters ranging from 9 to 28 nm. A total of 65 NPs were measured, yielding an average size of approximately 18.25 ± 0.07 nm. The AuNPs-Vo are predominantly spherical, and the size distribution shown in Fig. 4 (A, B and C) further confirms low polydispersity, where polydispersity is expected result for a biological synthesis, such as plant-based synthesis. The morphology observed through TEM indicates that short reaction times (<60 minutes) play a key role in forming spherical and pseudo-spherical nanoparticles [84]. This explains the results found for the optimized synthesis as well as the other syntheses in the factorial design, since all employed short reaction times. Chahardoli et al. [19] report that nearly spherical AuNPs are highly dispersed and small, ranging from 5 to 21 nm, corroborating the findings of this study. As shown in the TEM images, the high dispersion of AuNPs may be related to the efficiency of the compounds in the *Virola oleifera* extract in acting as stabilizing agents. Diksha et al. [30] correlated AuNP size

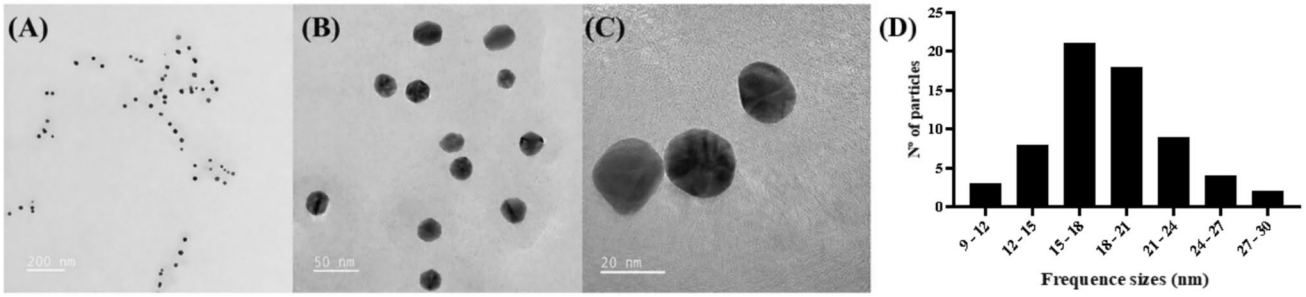


Fig. 4 Transmission electron microscopy (TEM) micrographs showing the morphology of gold nanoparticles synthesized from *Virola oleifera* (AuNPs–Vo) under optimized conditions determined by full factorial design (6 min reaction time, pH 8.3, extract concentration of 1.0 mg mL^{-1}). Images were acquired at magnifications of 200,000× (**A**), 50,000× (**B**), and 20,000× (**C**). The corresponding particle size distribution, determined using ImageJ® software, is also shown (**D**), and the graph was generated using GraphPad Prism 8.0 software (GraphPad Software Inc., San Diego, CA, USA)

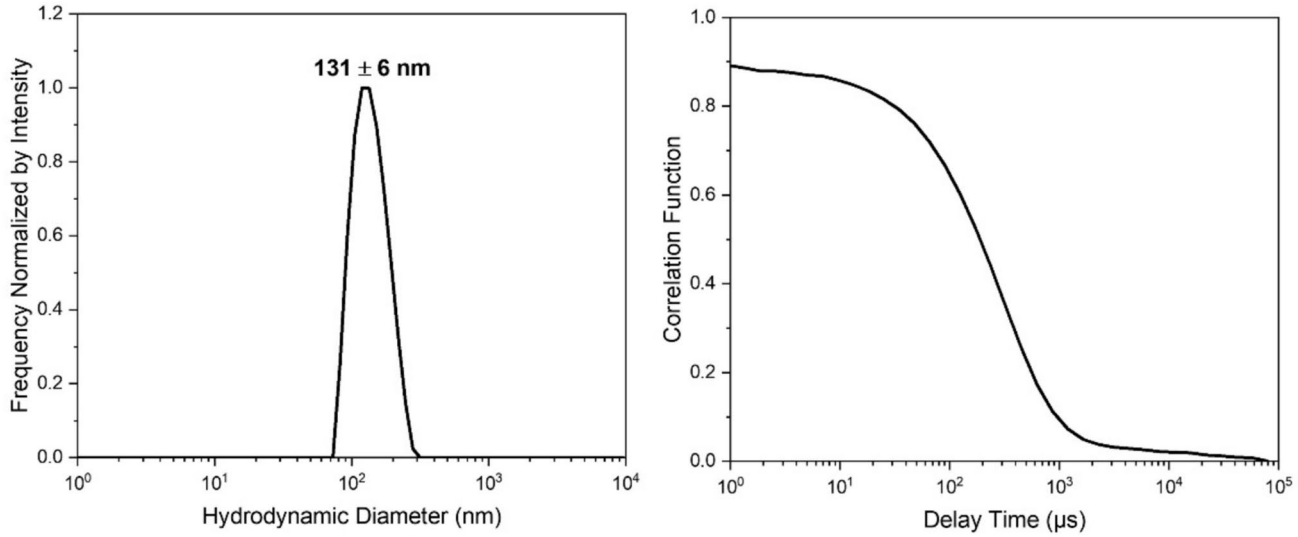


Fig. 5 Dynamic light scattering (DLS) spectra showing the hydrodynamic size distribution and colloidal stability (value ± standard deviation) of *Virola oleifera* gold nanoparticles (AuNPs–Vo), with graphs generated using OriginPro 8.5 software (OriginLab Corporation, Northampton, MA, USA)

with LSPR bands, showing bands between 527–535 nm corresponding to spherical nanoparticles with sizes of approximately 30–50 nm as observed in TEM images. Although their nanoparticles were larger than those obtained in this work, the spherical shape agrees with the wavelength range observed in this study. As presented by Bastús et al. [13] the larger the size of the AuNPs, the greater the LSPR band shift occurs at longer wavelengths.

Dynamic light scattering and Zeta potential assessments

The DLS measurements indicate the hydrodynamic diameter of AuNPs-Vo in aqueous medium, and the value around 131±6 nm provides information on about water solvation, metallic cores, as well as any biological molecules bound to or adsorbed on the particle surfaces (electrical double layer). This explains why the particle size measured by DLS is larger than the values obtained by TEM [24]. The sample polydispersity index (PI) was evaluated employing the cumulant method, resulting in a value of about 0.5 ± 0.1 (Fig. 5). Polydispersity index values from 0.4 indicate that the samples exhibit polydispersity. The PI value obtained for the AuNPs-Vo corroborates the polydispersity observed in the TEM images [55].

The zeta potential (ZP), can supply information on the surface charge of nanomaterials, as well as on colloidal stability. The ZP value obtained for the AuNPs-Vo was about -46 ± 3 mV, indicating that the surface is negatively charged. Regarding colloidal stability, colloids with ZP values greater than ±25 mV are considered stable [41], while colloids with absolute ZP values above 30 mV as highly stable and those below 10 mV, neutral [25]. As long as the ZP remains above +30 mV or below −30 mV, NPs remain stable. Surface charge prevents particle aggregation [45].

However, it is important to note that the stability of AuNPs-Vo may also be related to the steric hindrance promoted by other compounds present in the sample. The surface charge measured by ZP are likely related to the pH of the extract used in the synthesis (pH 8.3), which is slightly alkaline. This pH deprotonates hydroxyl groups in the plant compounds (flavonoids, phenols, and alcohols), which not only facilitate the bioreduction of Au during synthesis [84],but also promote negatively charged AuNPs with enhanced capping and stabilization [42].

The synthesized AuNPs exhibited a highly negative zeta potential (-46 mV) at the pH (8.3) synthesis, indicating strong electrostatic repulsion between particles and excellent colloidal stability (Clogston; Patri, 2011). Generally, absolute zeta potential values above 30 mV are considered indicative of highly stable nanosuspensions due to sufficient repulsive forces preventing aggregation [78]. Since the particles remained stable over a broad pH range (3–9), including values close to physiological conditions, it is reasonable to infer preservation of colloidal stability at physiological pH (~7). Similar behavior has been reported for plant-mediated AuNPs, in which colloidal stability is retained near neutral pH because biomolecules adsorbed on the nanoparticle surface provide both electrostatic and steric stabilization [81].

For biomedical applications, however, nanoparticle behavior under physiological conditions is influenced not only by pH but also by ionic strength and biomolecular interactions. In electrolyte-rich media such as PBS or cell culture medium, ion screening may reduce electrostatic repulsion, while protein corona formation can alter hydrodynamic size and surface charge [41]. Therefore, although the present pH stability results support potential physiological stability at neutral pH, future studies evaluating zeta potential and hydrodynamic diameter directly in simulated physiological media are warranted.

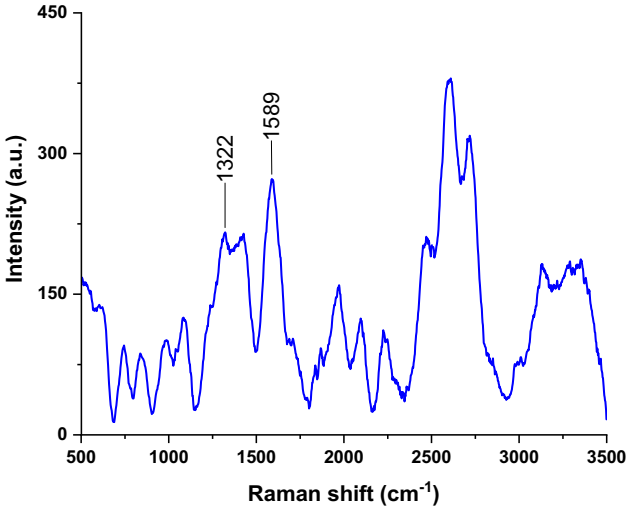


Fig. 6 SERS spectrum of gold nanoparticles synthesized using *Virola oleifera* extract (AuNPs-Vo), highlighting the bands at 1322 and 1589 cm^{-1}, which are consistent with signals previously reported in the literature for AuNPs synthesized with *Virola oleifera* extract (https://doi.org/10.1186/s11671-016-1683-3). Graphs were generated using OriginPro 8.5 software (OriginLab Corporation, Northampton, MA, USA)

Surface-Enhanced Raman Scattering (SERS) analysis

Surface-enhanced Raman scattering (SERS) spectroscopy was employed to investigate the molecules adsorbed onto the surface of gold nanoparticles synthesized by reduction with *Virola oleifera* extract (AuNPs-Vo) (Fig. 6). Unlike the conventional Raman spectra reported in the literature [65], additional bands and higher spectral intensities were observed, which can be attributed to the SERS effect arising from the interaction between phenolic compounds from the extract and the plasmonic surface of the AuNPs [62]. The SERS spectrum exhibited intense bands at approximately 1322 and 1589 cm^{-1}, in agreement with signals previously reported for AuNPs synthesized using *Virola oleifera* extract (Nascimento-Dias, 2025). The band at 1322 cm^{-1} can be attributed to the symmetric stretching mode of carboxylate groups (COO^-), whereas the band at 1589 cm^{-1} is associated with the asymmetric stretching of the same groups [31]. In addition, bands observed between 2800–3350 cm^{-1} were associated with C–H stretching modes of aromatic and aliphatic organic compounds [16]. Therefore, the identified functional groups can be attributed to the abundance of polyphenolic molecules from the *Virola oleifera* extract present on the surface of the AuNPs. These results corroborate those obtained from other characterization techniques and provide additional information regarding surface-bound molecules with high antioxidant potential.

Gold determinations

The Au concentrations as determined by ICP-OES in the three synthesis AuNPs-Vo 23, 21 and 21 mg mL^{-1}) were lower than in the $HAuCl_4$ solution (25 mg mL^{-1}). This difference is hypothesized to result from material loss during the washing steps, although the reduction was not statistically significant. Similar results were reported in previous studies by De Resende Marques et al. [29] employing ICP-MS on the same AuNPs-Vo. Even under different synthesis conditions (pH 7.7 and extract concentration 0.5 mg mL^{-1}), the gold concentration in the nanomaterials was 0.019 mg mL^{-1}, equivalent to 9.9×10^{-5} mol L^{-1} Au, suggesting that optimized AuNPs-Vo solutions can maintain similar gold concentrations, and that these concentrations remain consistent across different Au detection techniques.

Flocculation analysis

The flocculation results show that the area AUC values increase proportionally with NaCl concentration, indicating greater aggregation of AuNPs-Vo compared to the control (0.67). Specifically, AUC values rose to 0.8, and 0.91 for NaCl concentrations of 100, and 200 mmol L^{-1}, respectively (Fig. 7A). Regarding pH effects (Fig. 7C), significant changes in AUC relative to the control were observed at both acidic (pH 1: 0.74; pH 2: 0.73) and basic (pH 12: 0.76; pH 13: 1.09) extremes, demonstrating that extreme pH values can alter nanoparticle aggregation states. Regarding the NaCl results, solutions with higher salt concentrations contain greater amounts of Na^+ ions. The positive charge of these ions can form ionic interactions with the negatively charged AuNPs-Vo, promoting increased cluster formation (aggregated particles) and consequently raising the AUC values.

The pH graph (Fig. 7C) shows the same'values under highly acidic and highly basic conditions. Two possible explanations can account for this: first, a higher concentration of cationic H^+ particles may interact with anionic organic molecules on the AuNPs-Vo surface; second, anionic particles such as Cl^- and OH^- may induce electrostatic repulsion between AuNPs-Vo, leading to greater nanoparticle aggregation and a subsequent higher in AUC compared to the control.

For temperature (°C) (Fig. 7B), no significant differences were observed between the control and the tested temperatures. However, the AUC value of nanomaterials subjected to autoclaving (0.79) was significantly higher than that of the control (0.67), suggesting that pressure was likely the main factor behind this observation.

As metallic nanoparticles, AuNPs-Vo possess intramolecular ionic bonds in their structure. Additional interactions, such as hydrogen bonds, are also possible because the compounds identified in the extract contain hydroxyl and amino groups capable of forming these bonds. Both ionic and hydrogen bonds are strong and can provide resistance to the nanomaterials under the tested temperatures and autoclaving pressures, which explains the observed results. This hypothesis is supported by Souto et al. [81], who discussed primary bonds formed in polymeric NP synthesis, composed of hydrogen bonds that ensure nanoparticle stability. Similarly, Ganesan et al. [41] demonstrated the robustness of these bonds in resistance tests using AuNP-functionalized cotton fibers, obtaining positive results.

Statistical analyses

Statistical analyses in the characterization processes were selected according to the number of experimental groups and the ami of each analysis. Student's t-test was applied to compare only two groups, allowing the identification of statistically significant differences between the means. A one-way analysis of variance (ANOVA) was used to compare three or more groups, as it allows for the simultaneous evaluation of differences between multiple experimental conditions, reducing the risk of type I error associated with multiple pairwise comparisons. When the ANOVA indicated significant differences, appropriate *post-hoc* analyses were performed to identify which groups differed significantly. These approaches were adopted to ensure a robust statistical interpretation of the physicochemical and biological characterization data.

Cytotoxicity assessments

Cytotoxicity was assessed following the standardized ISO 10993–5 (2009) [51] protocol, which classifies a substance as cytotoxic when cell viability is <70% compared to the untreated control. It was observed that the AuNPs-Vo were

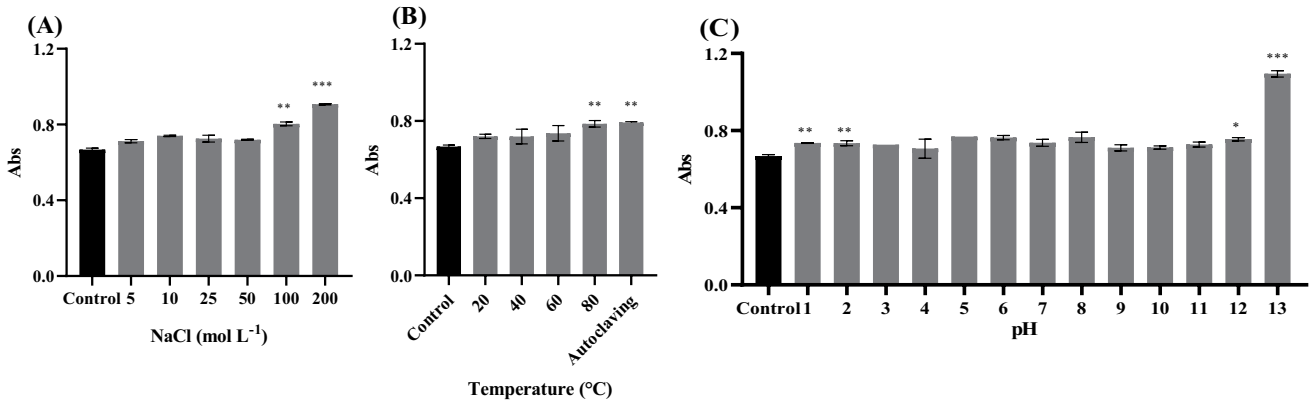


Fig. 7 Absorbance at 600 nm expressed as area under the curve (AUC), illustrating the flocculation behavior of *Virola oleifera* gold nanoparticles (AuNPs–Vo) under different NaCl concentrations (**A**), temperatures (**B**), and pH values (**C**), relative to the control. Data are presented as mean ± standard deviation. Statistical significance is indicated as *p < 0.05, ***p < 0.001, and ****p < 0.0001 compared with the control group. Graphs were generated using GraphPad Prism 8.0 software (GraphPad Software Inc., San Diego, CA, USA)

advantageous compared to their individual components in terms of cytotoxicity (Fig. 8A and B), as exposure to the nanoparticles led to higher cell survival at both exposure times (24 h and 96 h) [47]. Cells exposed to AuNPs-Vo at concentrations of 50, 30, and 10 mg mL^{-1} (N100, N60, and N20) showed viability rates above 85% at 24 h and 77.5%, 87.6%, and 91.8%, respectively, at 96 h. Exposure to the extract resulted in variable survival rates. No cell death was observed at concentrations of 1.0 and 0.2 mg mL^{-1} (E100 and E20), while a 0.6 mg mL^{-1} concentration (E60) led to 64.19% survival at 24 h. At 96 h, the same concentrations resulted in survival rates of 57% and 79%, respectively. Notably, exposure to 1.0 mg mL^{-1} extract (E100) caused only 17% survival at 96 h, indicating high toxicity with viability significantly below 50%. Cells exposed to different concentrations of $HAuCl_4$ showed survival rates similar to those of AuNPs-Vo, with 89.5% survival for 0.085 mg mL^{-1} (O100) and 77.8% for 0.017 mg mL^{-1} (O20) at 96 h. At 24 h, survival was 99% for both concentrations. However, higher concentrations of $HAuCl_4$ (0.051 mg mL^{-1}, O60) led to a marked decrease in cell viability (56.7% at 96 h), highlighting the importance of carefully evaluating the cytotoxicity of this reagent. All described results can be observed in the optical electron microscopy images, which show the changes in the cells compared to the control (Fig. 9C), in which those exposed to the materials that resulted in the lowest survival percentages (E100, E60, E20 and O100) exhibited greater morphological changes (Fig. 9E100, E60, E20 and O100).

Dunn's test, comparing concentrations at different exposure times, revealed that only the extract at 1.0 mg mL^{-1} (E100) and $HAuCl_4$ at 0.051 mg mL^{-1} (O60) caused significant reductions in cell viability compared to the control. Aspects such as size, shape, surface charge, and aggregation state are crucial for determining the cytotoxicity of nanoparticles (NPs). NPs larger than 15 nm – such as AuNPs-Vo with sizes between 15 and 25 nm – exhibit low cytotoxicity because their cellular internalization is slower and more limited [79]. The lower survival percentage at E60 compared to E100 may be related to the complex chemical extract composition, in which metabolites with distinct properties can interact antagonistically or synergistically [17]. Furthermore, at higher concentrations, physicochemical changes such as molecular aggregation, partial compound precipitation, or reduced bioavailability can decrease direct interaction with cells, resulting in a less pronounced cytotoxic effect than at intermediate concentrations [33]. Similar non-monotonic responses have been reported in plant-mediated gold nanoparticle systems, in which intermediate concentrations may exhibit higher biological activity than more concentrated formulations. Rodríguez-León et al. [73] reported that biosynthesized AuNPs, using "jurema-preta" (*Mimosa tenuiflora*) extract, may show concentration-dependent changes in cytotoxicity due to aggregation and altered cellular uptake. Likewise, studies using phytochemical-mediated AuNPs using Brazilian red propolis have demonstrated that increasing extract concentration does not necessarily increase toxicity, as excess biomolecules may alter colloidal stability, reduce nanoparticle bioavailability, or promote biomolecule adsorption and protein corona formation in culture medium [15]. Therefore, the lower toxicity observed for E100 may reflect physicochemical changes that reduce

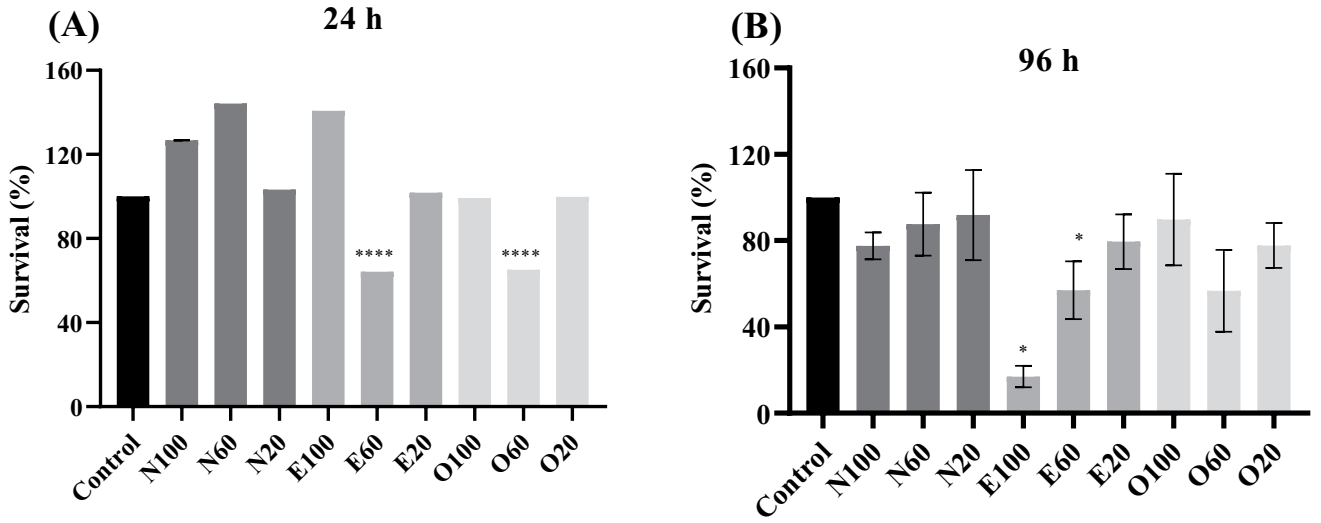


Fig. 8 Vero cell viability (%) determined by the MTT assay after 24 h (**A**) and 96 h (**B**) of exposure to different concentrations of AuNPs–Vo (N100, N60, and N20), aqueous extract (E100, E60, and E20), and $HAuCl_4$ (O100, O60, and O20). The control group corresponds to cells exposed to ultrapure water. Data are presented as mean ± standard deviation. Statistical significance is indicated as *$p < 0.05$, ***$p < 0.001$, and ****$p < 0.0001$ compared with the control group. Graphs were generated using GraphPad Prism 8.0 software (GraphPad Software Inc., San Diego, CA, USA)

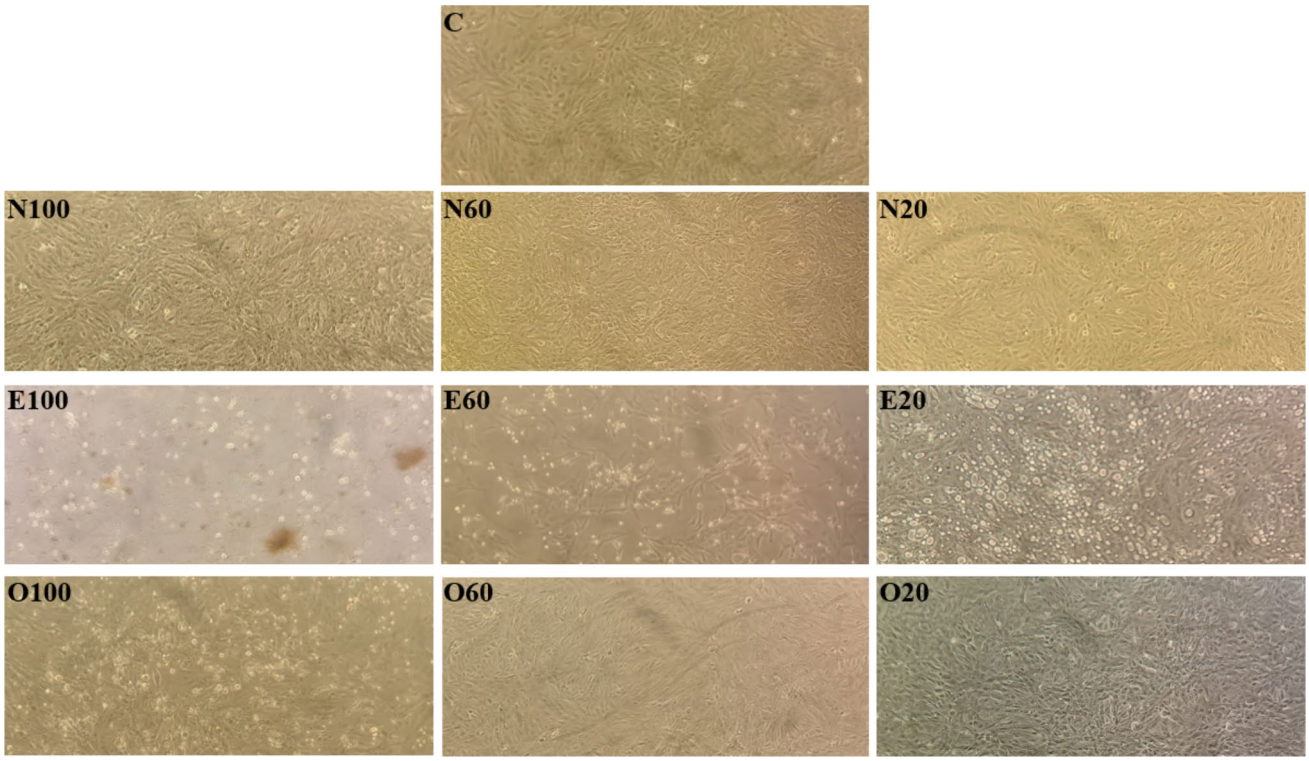


Fig. 9 Images of VERO cells after 96 h of exposure to AuNPs–Vo (N100, N60, and N20), aqueous extract (E100, E60, and E20), $HAuCl_4$ (O100, O60, and O20), and control (C), observed under an inverted optical microscope at 100× magnification (10× objective and 10× eyepiece). The images were photographed using a cellphone Samsung S23FE camera

effective cell–nanoparticle interaction rather than a conventional dose-dependent response.

Regarding surface charge, anionic NPs such as AuNPs-Vo have a low ability to disrupt cell membranes. This effect has been discussed by Albanese and Chan [3], who report that anionic NPs generally exhibit lower toxicity. This is explained by the poor adhesion and absorption of anionic systems on eukaryotic cell membranes, which are negatively charged, due to electrostatic repulsion forces [54]. This observation is corroborated in the present study, as AuNPs-Vo consist of gold atoms aggregated with various compounds, making them larger than the individual components dispersed in the extract. Qais et al. [70] confirm that AuNPs have a considerably higher percentage of atoms on their surface, and Cheng et al. [23] state that this characteristic renders AuNPs more selective and safer. Finally, the washing process of AuNPs-Vo also contributed to removing other components that, besides being smaller in size, could carry positive charges, potentially interacting with cells and causing membrane lysis.

Both the AuNPs-Vo and their aqueous extract exhibited high antioxidant capacity, with average results of 86.43% for the AuNPs-Vo and 55.13% for the extract. The IC_{50} values were 1684.31 µmol mL^{-1} and 1480.54 µmol mL^{-1}, respectively. These results indicate that the nanomaterial possesses a higher antioxidant potential than its extract, with a lower IC_{50}. The antioxidant molecules (phytochemicals) responsible for reducing Au^{3+} ions also contribute to the high activity of the nanomaterial. This is consistent with previous studies by Godipurge et al. [44] and Lin et al. [58] in which polyphenolic compounds responsible for the reduction of Au and Ag in nanoparticles also demonstrated antioxidant activity. Mechanistically, plant biomolecules such as phenols and flavonoids are generally nucleophilic due to their aromatic rings and are responsible for chelating potential [58]. Their interactions are responsible for reducing $HAuCl_4$ during the formation of AuNPs [19]. Thus, the AuNPs carry a high concentration of antioxidant molecules on their surface, which ensures their elevated antioxidant potential. This characteristic explains why the nanoparticles exhibit higher activity than the corresponding aqueous extract.

Oxidative stress biomarker assessments

Reduced glutathione (GSH) and glutathione S-transferase (GST) determinations

The statistical analyses of the oxidative stress assays corroborate the results observed in the MTT tests, since cells

exposed to different extract concentrations and to the O60 concentration of $HAuCl_4$ also exhibited statistically higher production of molecules recognized as oxidative stress biomarkers (Fig. 10). Cells exposed to different AuNPs-Vo concentrations did not present significant GSH level changes compared to the control at either time point. However, cells exposed to $HAuCl_4$ concentrations O100 at 24 h (Fig. 10A) presented significant alterations indicating oxidative processes. In terms of GSH quantification, changes in enzyme metabolism are associated with increased oxidative stress, with a strong correlation between reduced GSH levels and enzymatic defense mechanisms [21]. Studies by Zhang et al., [89] reported the main kinetic parameters of reduced glutathione and proposed catalytic mechanisms for this enzyme involving its key substrates, glutathione and hydrogen peroxide. Different types of GSH are known to promote the reduction of hydroperoxides derived from lipid complexes such as cholesterol, even when these peroxides are present within the cell membrane [69]. In the present study, the GSH assay results from the cytotoxicity experiments are consistent with the literature (Fig. 9B). At 96 h, the significant increase in enzyme levels in cells exposed to the extract (E20) and $HAuCl_4$ (O20), compared to the control, indicates a substantial degree of lipid peroxidation.

In healthy tissues, approximately 90% of glutathione exists in its reduced form, which protects cells by removing reactive metabolites through conjugation with these reactive species [21].

Oxidative stress is inversely proportional to GSH concentration in organisms when it is present in its oxidized form [11]. In humans, elevated GSH levels are associated with several diseases, including cancer, neurodegenerative disorders, and cardiovascular diseases, making it a highly sensitive indicator of cellular functionality and viability [89]. In the present findings, it is hypothesized that GSH fulfilled its antioxidant role by protecting cells exposed to all concentrations of the extract and $HAuCl_4$, as its increase was related to its reaction with the reactive oxygen species

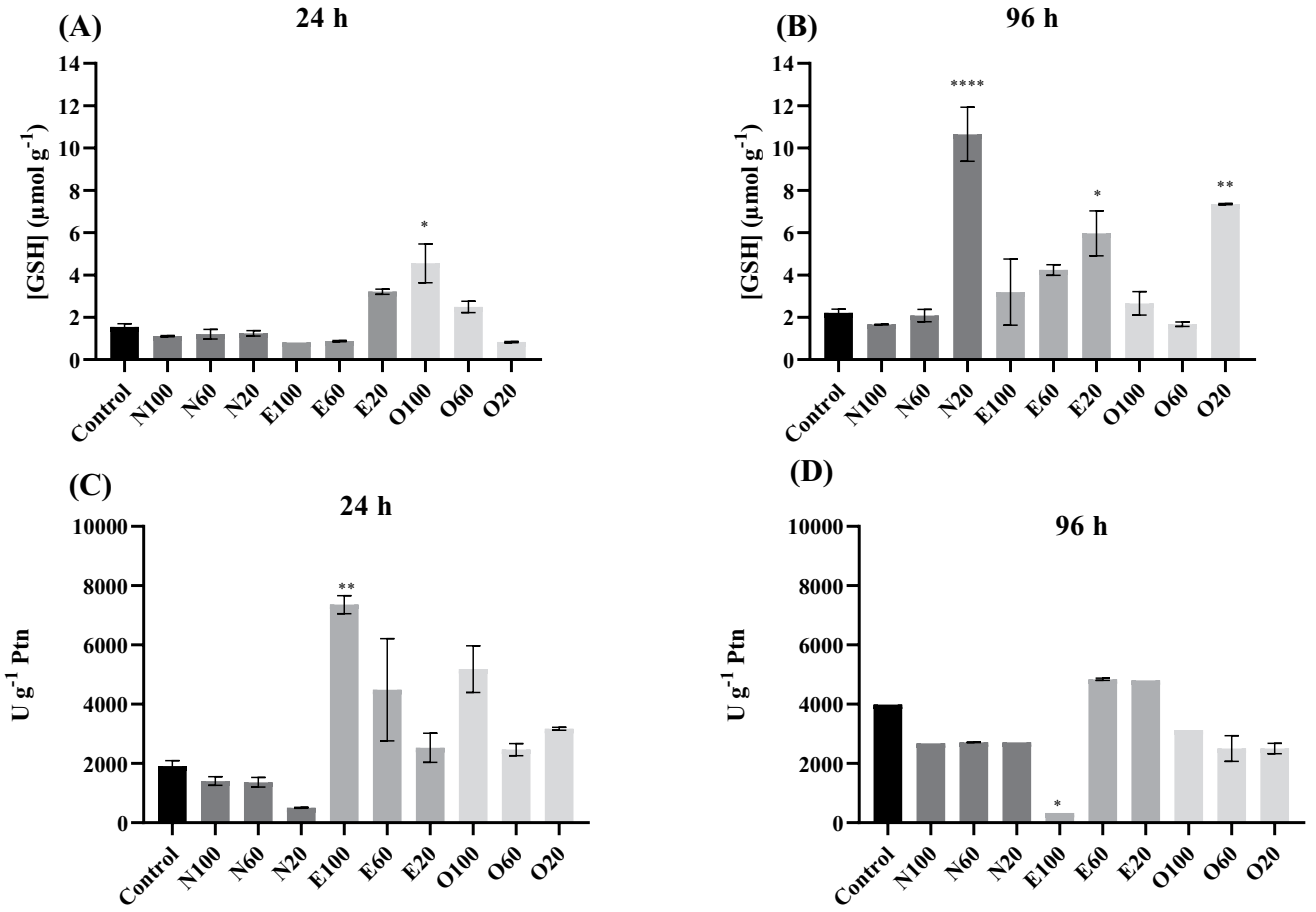


Figure 10. Intracellular reduced glutathione (GSH) levels (**A**, **B**) and glutathione S-transferase (GST) activity (**C**, **D**) in cells treated with different concentrations of *Virola oleifera* gold nanoparticles (AuNPs–Vo) (N100, N60, and N20), aqueous extract (E100, E60, and E20), and $HAuCl_4$ (O100, O60, and O20) at different exposure times, compared with control cells. Data are presented as mean ± standard deviation. Statistical significance is indicated as *p < 0.05, **p < 0.001, and ***p < 0.0001 compared with the control group. The limits achieved by the GSH method were 0.7 µmol g^{-1} for the Limit of Detection and 2.2 µmol g^{-1} for the Limit of Quantification. Graphs were generated using GraphPad Prism 8.0 software (GraphPad Software Inc., San Diego, CA, USA)

(ROS) present in the exposed cells [69]. Regarding GST, no changes were noted in any of the cells exposed to all nanoparticle concentrations at either exposure time. However, the significant decrease in GST observed for concentration N20 at 24 h suggests that the cells experienced oxidative protection, likely due to antioxidant molecules present on the nanomaterial surface. Conversely, cells exposed to concentration E100 and gold showed a marked and significant increase in GST levels compared to the control at 24 h, indicating oxidative damage (Fig. 10C), and after, decrease was drastically reduced over the 96-hour period (Fig. 10D), suggesting that this decrease over time is related to enzyme saturation in the presence of ROS. Both GSH and GST concentrations increased significantly in cells exposed to the extract and gold precursor, conditions that also resulted in lower cell survival rates. This occurred because proteins of the GST superfamily play a key role in detoxifying many endogenous compounds and breaking down xenobiotic substrates through the conjugation of GSH's electrophilic substrates, in addition to regulating the oxidative stress response [88]. In detail, the increase in GST in these exposures is mainly due to its peroxidase activity and detoxifying function in the cytosol, serving as a binding protein for a wide range of organic substances, such as cytotoxic products of lipid peroxidation, including lipid hydroperoxides and reactive carbonyls [7].

Hydrogen peroxide (H_2O_2) and Catalase (CAT) determinations

Concerning H_2O_2, compared to the control, cells exposed to the highest extract concentration showed a fourfold increase in H_2O_2, while those exposed to the intermediate concentration showed a twofold increase (Fig. 11). This is consistent with the GST assays, in which the same treatments led to elevated GST levels, suggesting that this increase is related to a detoxification process, as previously reported in the literature. Conversely, cells exposed to AuNPs and $HAuCl_4$ did not show significant changes in peroxide concentration. Although different $HAuCl_4$ exposures resulted in significantly increased GST activity, the descriptive results suggest that this increase was not associated with elevated peroxide levels. It is also noteworthy that cells exposed to different AuNPs concentrations exhibited reduced GST activity, indicating that the nanomaterials may exert a protective effect. This protective effect could be attributed to the plant-derived surface molecules responsible not only for reducing gold ions during synthesis but also for promoting antioxidant activity in cells, such as vitamins A (retinol), C (L-ascorbic acid), and E (α-tocopherol). This type of non-enzymatic protection prevents lipid peroxidation and ensures an efficient radical-scavenging capacity under physiological conditions [21].

Catalase activity indicated that most of the significant changes coincided with variations in H_2O_2 concentrations, demonstrating an inverse relationship between the two parameters (Fig. 11A). It was observed that in cells treated with E60 at 24 h, CAT activity decreased by 56.61%, while H_2O_2 concentration in the same group increased by 138.02%. A similar trend was noted for the E100 and E20 treatments at 96 h (Fig. 11B); in the first case, CAT decreased by 26.97%, while in the second it increased by 258.77% corresponding to H_2O_2 concentrations that increased by 203.21% and decreased by 68.31%, respectively. Significant changes in CAT activity were also observed in cells exposed to N100 at both exposure times, showing decreases of 28.36% and 80.59% at 24 h and 96 h, respectively. Similarly, in cells exposed to E100, O60, and O20 at 96 h, CAT activity decreased by 26.97%, 22.19%, and 43.03%, respectively. However, based on the data, these decreases do not appear to be directly correlated with increases in cellular H_2O_2 concentrations, but rather may be influenced by other factors. In the case of cells exposed to E100, for instance, there was a noticeable consumption of GST, and the concurrent reduction in CAT activity may suggest a compensatory or synergistic interaction between these enzymes. This indicates that the antioxidant defense system may be dynamically balancing enzymatic activities to counteract oxidative stress and maintain redox homeostasis within the cells [52].

In contrast, in cells exposed to O60 and O20, where a significant increase in carbonylated proteins was observed, the consumption of CAT in these cases may be associated with the enzyme's role in counteracting oxidation processes occurring in those cells (Fig. 11C and D). CAT is responsible for converting hydrogen peroxide into water, thereby preventing the cascade of reactions that generate new oxidative byproducts through successive single-electron reductions of reactive intermediates (Jesus et al., 2020). Among the consequences of such cascades, the excessive production of these radicals, often resulting from persistent pathological processes—can overwhelm antioxidant defense mechanisms and lead to direct tissue damage, lipid peroxidation of cellular membranes, and protein carbonylation [38].

Lipid peroxidation (MDA) and carbonylated protein (PTC) determinations

Regarding lipid peroxidation assays, after 24 hours (Fig. 12A), a significant decrease in MDA levels was observed compared to the control in cells exposed to the AuNPs-Vo concentrations of N60 and N20, as well as in cells exposed to $HAuCl_4$ concentrations O100. After 96 hours (Fig. 12B), a significant increase occurred in all cells exposed to the

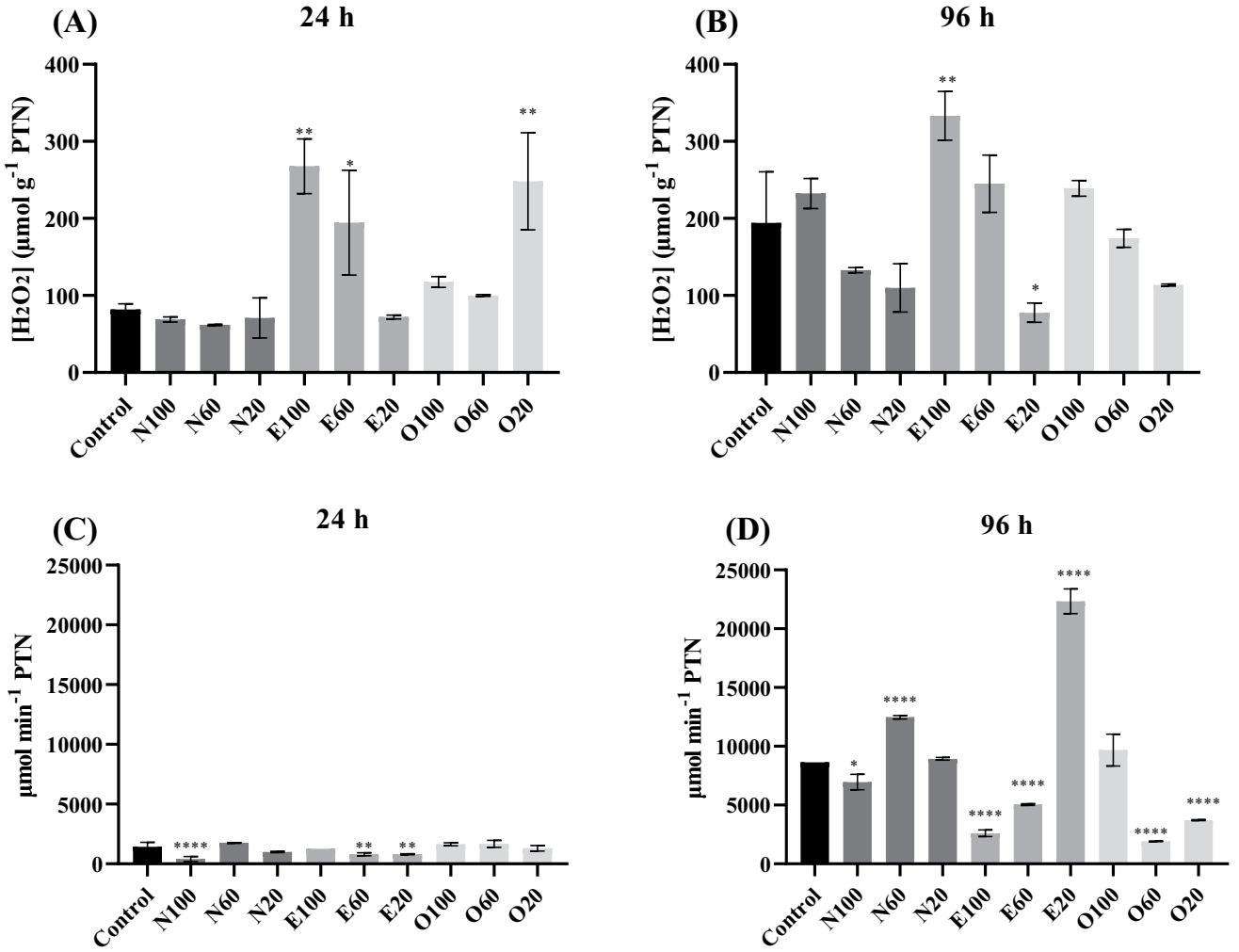


Fig. 11 Intracellular hydrogen peroxide (H_2O_2) levels (**A**, **B**) and CAT activity (**C**, **D**) in cells treated with different concentrations of *Virola oleifera* gold nanoparticles (AuNPs–Vo) (N100, N60, and N20), aqueous extract (E100, E60, and E20), and $HAuCl_4$ (O100, O60, and O20) at different exposure times, compared with control cells. Data are presented as mean ± standard deviation. Statistical significance is indicated as *p < 0.05, **p < 0.001, and ***p < 0.0001 compared with the control group. The limits achieved by the [H_2O_2] method were <0.0001 µmol g^{-1} for both the Limit of Detection and the Limit of Quantification. Graphs were generated using GraphPad Prism 8.0 software (GraphPad Software Inc., San Diego, CA, USA)

extract and AuNPs-Vo concentrations and to the O100 and O60. These findings are consistent with the MTT assay results, where the same exposure groups that showed elevated MDA levels also exhibited a higher percentage of cell death. MDA is a terminal compound of lipid peroxidation that serves as a marker of oxidative damage caused by reactive oxygen species. Peroxidative damage induced by oxygen free radicals leads to elevated MDA formation [18]. Lipid peroxidation is a cellular injury mechanism caused by free radicals or chemical agents that affect cell membranes, lipoproteins, and other lipid-containing molecules. This often results in irreversible cellular damage and is considered an early cause of cell death (Aloke; Onisuru; Achilonu, 2024). The outcomes of lipid peroxidation include structural damage to membranes and the generation of oxidized products—some of which are chemically reactive (such as lipid peroxyl radicals, hydroperoxides, and various oxidation products), that can covalently modify macromolecules, leading to tissue injury [6]. These uncontrolled reactions ultimately cause membrane rupture and cell death [27]. Conversely, the reduced levels of reacted MDA and carbonylation observed over time suggest that the molecules present in both the extract and the AuNPs-Vo acted as protective agents against the produced ROS. These molecules were identified by Aquino et al., [28] as ferulic acid, gallic acid, and quercetin, which have been described by Barreca [12] as antioxidant compounds. Their radical-scavenging mechanisms are attributed to their redox properties, as reported by Wadwa et al., [86].

Similar results were observed in the protein carbonyl assays (Fig. 12C), where cells exposed to different concentrations of the aqueous extract produced significantly higher

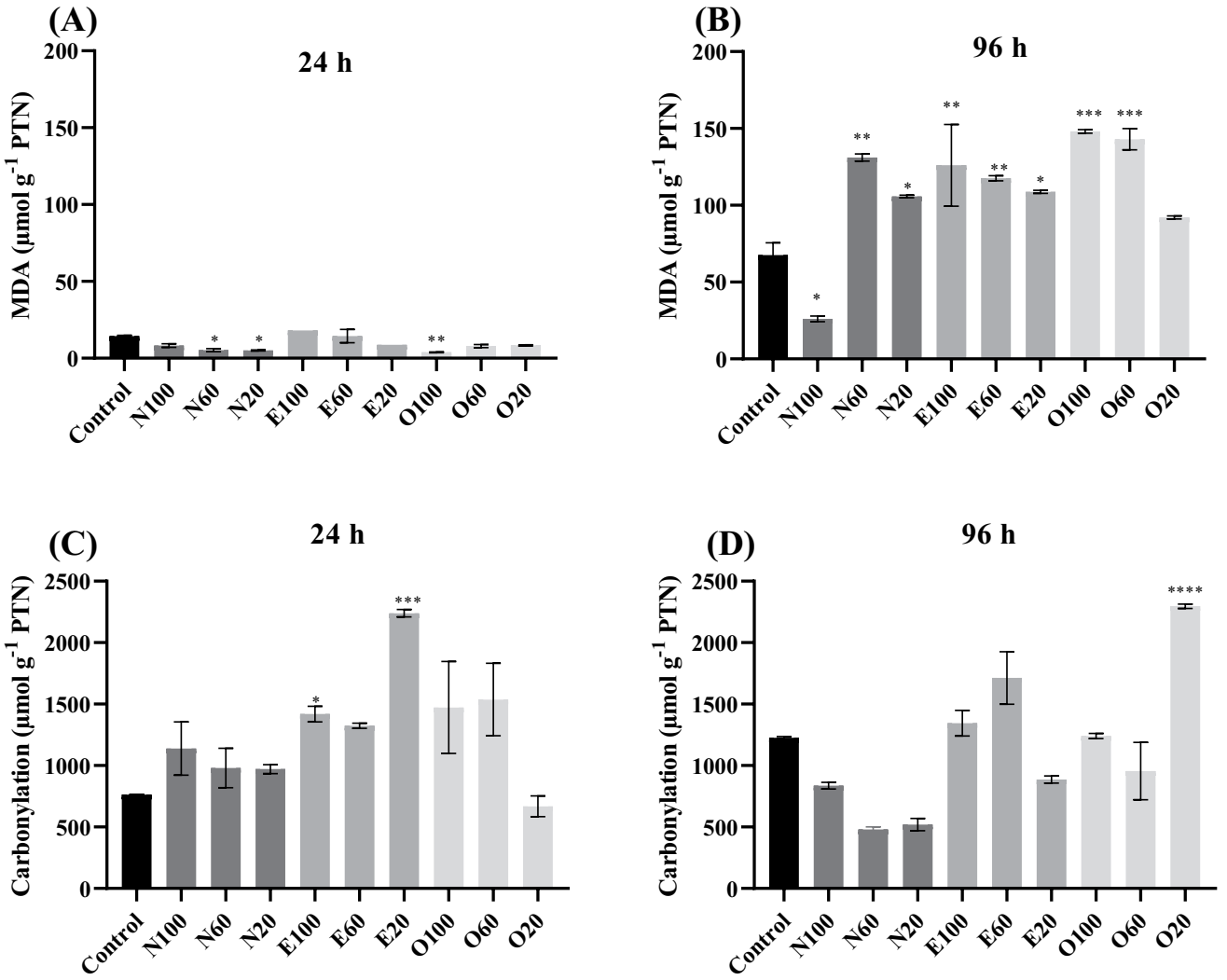


Fig. 12 Malondialdehyde (MDA) levels in cells after 24 h (**A**) and 96 h (**B**) and levels of carbonylated proteins in cells after 24 h (**C**) and 96 h (**D**) of exposure to different concentrations of *Virola oleifera* gold nanoparticles (AuNPs–Vo) (N100, N60, and N20), aqueous extract (E100, E60, and E20), and $HAuCl_4$ (O100, O60, and O20), compared with control cells. Data are presented as mean ± standard deviation. Statistical significance is indicated as *p < 0.05, ***p < 0.001, and ****p < 0.0001 compared with the control group. The limits achieved by the MDA method were 0.305 µmol g^{-1} for the Limit of Detectaion and 1.017 µmol g^{-1} for the Limit of Quantification. Graphs were generated using GraphPad Prism 8.0 software (GraphPad Software Inc., San Diego, CA, USA)

amounts of carbonylated proteins compared to the control at all concentrations after 24 hours. However, at 96 hours (Fig. 12D), the levels of protein carbonylation decreased overall, except in cells exposed to concentrations of O20, which showed significant increases. Conversely, cells exposed to O20 at 24 hours, as well as those treated with 60% and 20% (N60 and N20) concentrations of AuNPs-Vo at 96 hours, exhibited light decreases in protein carbonylation levels. Protein carbonylation reactions are also products of ROS activity, which oxidizes the alcohol groups of protein molecules, converting them into aldehydes, the chemical group corresponding to carbonyls [57]. These oxidative stress findings indicate that AuNPs-Vo cause less toxicity than their synthesis reagents when analyzing the high production of ROS. This can be explained by the higher concentration of compounds present in the aqueous extract, which were removed during the washing of the AuNPs. These compounds, in addition to having greater membrane reactivity and penetration, can generate ROS within cells.

Total antioxidant capacity (CAOT)

After 24 h (Fig. 13A) of exposure, a significant increase in CAOT was observed in groups E100 and O20 compared to the control, suggesting initial activation of the cellular antioxidant system. However, after 96 h (Fig. 13B), most treatments showed values close to the control or a reduction in CAOT, such as in treatments N20, E100, E60, and

E20, indicating possible antioxidant consumption or adaptation to induced oxidative stress. There was also a significant increase in treatments E100 and O60, indicating compensatory activation of the antioxidant system.

The results of this experiment are consistent with the biomarker analyses performed. The increase in treatments E100 and O20 at 24 h may be related to the adaptive response of cellular systems to the high concentrations of hydrogen peroxide found in Fig. 11; however, the increases in N100 and O60 at 96 h were not correlated with any alteration, suggesting only a higher concentration of antioxidant molecules present in the nanomaterial. The decreases found in N20 and in all extract treatments may be correlated with increased MDA concentrations.

Statistical analysis

Oxidative stress biomarkers correlations from PCA

A strong negative correlation was found between GSH and MDA (-0.496) at both time points, indicating antagonism. This means that higher concentrations of MDA, as an indicator of greater oxidative stress, resulted in greater activity of the antioxidant system (GSH) to control and reduce these high stress levels [36] and, consequently, its consumption, corroborating the results shown in experiments with cells exposed to all concentrations of extract and $HAuCl_4$. A strong positive correlation was observed between GSH and CAT (0.643), indicating that both increase or decrease concomitantly. From the experimental results, it is suggested that both increase in the presence of excessive ROS to protect the exposed cells [27], as exemplified by the cells exposed to concentrations of O100 at 24 h, N20, E20, and O20 at 96 h. A strong positive correlation was also found between GST and hydrogen peroxide concentration at 24 h (0.820), while a negative correlation was observed between hydrogen peroxide concentration and CAT at 96 h, indicating increased enzymatic activity to combat free radicals and degrade high H_2O_2 concentrations in cells. The same reasoning can explain the high positive correlation between MDA and CAT (0.523). Finally, another moderate negative correlation was found between GSH and hydrogen peroxide concentration at 96 h (-0.504), which could be explained by the greater consumption of GSH by cells that produced significant amounts of H_2O_2. In addition to MTT and carbonylated proteins (-0.35), indicating that protein carbonylation was a crucial factor in the decrease in cell viability. For CAOT, there was no significant correlation, highlighting a null correlation between it and GST activity.

Concerning the PCA (Fig. 14), GSH, MDA, and CAT occupy the same quadrant, pointing in similar directions with small angles between their vectors. This indicates directly proportional increases and decreases, consistent with the positive correlations identified among these biomarkers. A similar pattern is observed for GST and H_2O_2. The GSH vector, however, is nearly perpendicular (90°) to the vectors representing protein carbonylation, GST, and H_2O_2, suggesting little or no linear correlation with these variables. Nonetheless, when compared with the Spearman correlation, moderate associations are evident.

Concerning the relative contribution of biomarkers to explaining the observed results, most vectors extend

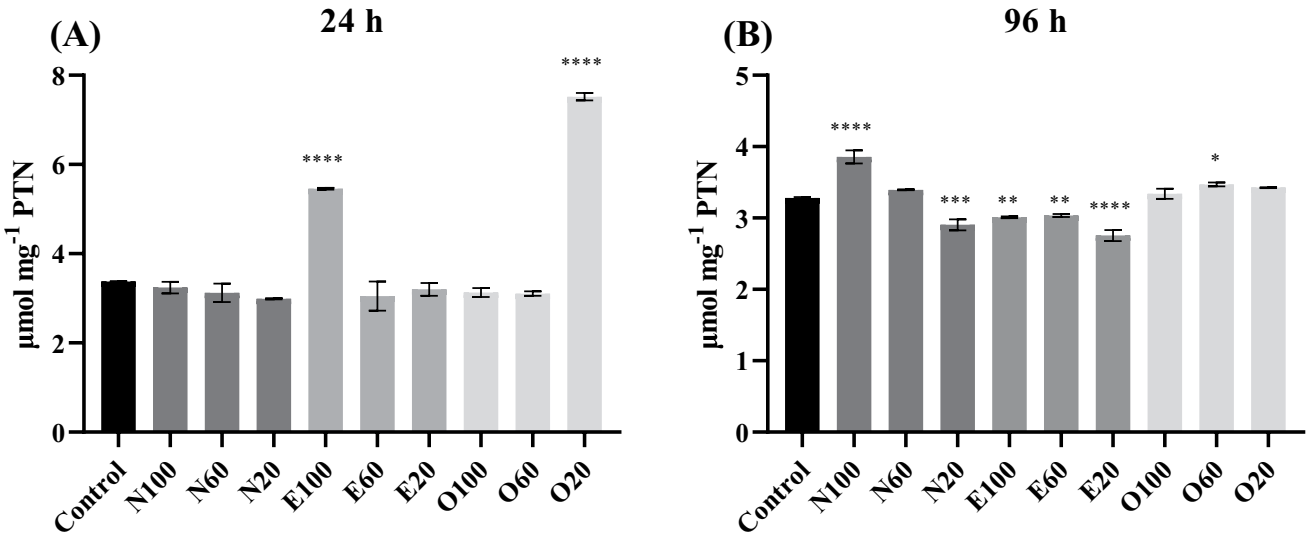


Fig. 13 Total oxidative cation exchange capacity (CAOT) levels in cells after 24 h (**A**) and 96 h (**B**) and levels of carbonylated proteins in cells after 24 h (**C**) and 96 h (**D**) of exposure to different concentrations of *Virola oleifera* gold nanoparticles (AuNPs–Vo) (N100, N60, and N20), aqueous extract (E100, E60, and E20), and $HAuCl_4$ (O100, O60, and O20), compared with control cells. Data are presented as mean ± standard deviation. Statistical significance is indicated as *$p < 0.05$, ***$p < 0.001$, and ****$p < 0.0001$ compared with the control group. Graphs were generated using GraphPad Prism 8.0 software (GraphPad Software Inc., San Diego, CA, USA)

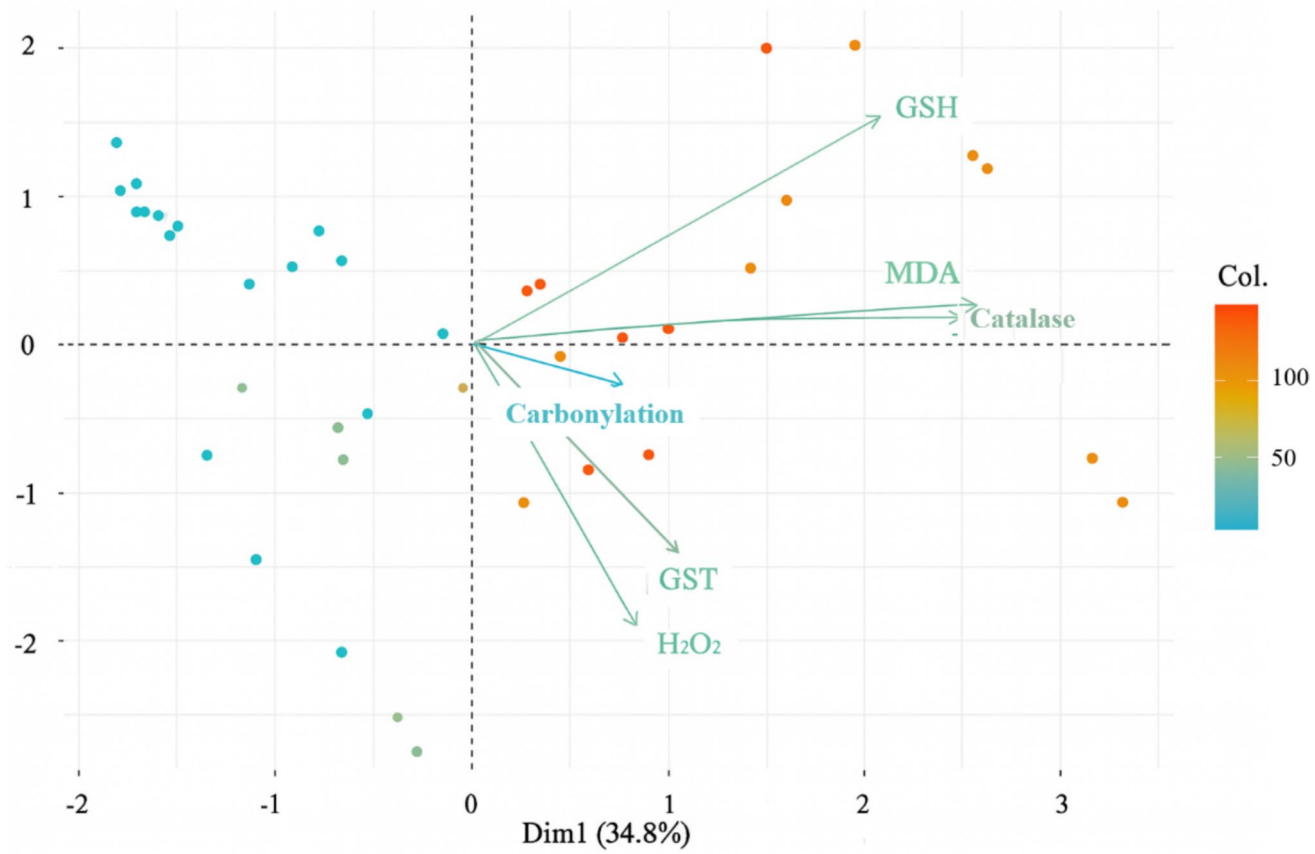


Fig. 14 Biplot of Principal Component Analysis (PCA) of oxidative stress biomarkers *of the cellular samples subjected to the control and different treatments of AuNPs-Vo (N100, N60 and N20), extracts (E100, E60 and E20) and $HAuCl_4$ (O100, O60 and O20)*. The points represent the experimental samples, colored according to the variable "Col." (color gradient shown on the right). The arrows indicate the contribution vectors of the biochemical variables: reduced glutathione (GSH), malondialdehyde (MDA), catalase, glutathione S-transferase (GST), hydrogen peroxide (H_2O_2), and protein carbonylation. The length and direction of the vectors reflect the magnitude and direction of the correlation of the variables with the principal components. PCA analysis and graph construction were performed using RStudio software (RStudio Team, Boston, MA, USA)

substantially from the origin. GSH, MDA, CAT, and protein carbonylation are the most influential in shaping and separating the data along the two dimensions, as indicated by their reddish-orange coloration. In contrast, GST and H_2O_2 exhibit minimal contributions, reflected by their bluish vectors. GSH, MDA, and CAT are located in the upper right quadrant, indicating a state in which both oxidative damage (MDA) and antioxidant defenses (GSH, CAT) are high. Conversely, GST and H_2O_2 occupy the lower left quadrant, reflecting a state where H_2O_2 and GST are positively correlated and negatively correlated with GSH, MDA, and CAT along Dimension 1. Protein carbonylation is positioned in the upper left quadrant, negatively correlated with Dimension 1 and positively correlated with Dimension 2.

Colored points represent control and exposed cell samples. Orange points, predominantly in the upper right quadrant (Dim1 > 0, Dim2 > 0), indicate samples with high levels of GSH, MDA, and CAT compared to others, likely corresponding to cells exposed to concentrations N60, N20, and E20 at 96 h, which exhibited high oxidative stress and antioxidant defense profiles. Brighter orange points in right quadrants likely reflect treatments inducing increased MDA and enhanced GSH and CAT defenses, as observed in cells exposed to E20, O100, O60 at 24 h, N60, and all extract and $HAuCl_4$ concentrations at 96 h.

Green points clustered in the upper and lower left quadrants (Dim1 < 0) correspond to samples with low GSH, MDA, and CAT levels but elevated carbonylated protein levels, consistent with cells exposed to E20 at 24 h and E60 and O20 at 96 h. Blue points represent profiles negatively correlated with the first group along Dimension 1 and slightly dispersed along Dimension 2, indicating samples with higher GST and H_2O_2 or elevated carbonylated proteins, such as cells exposed to E60 at 24 h and E100 at 96 h. The positioning of E60 at 24 h is consistent with the reduced cell viability observed in the MTT assay, in which E60 induced lower survival than E100. This non-linear concentration-response may indicate that E60 represents an intermediate

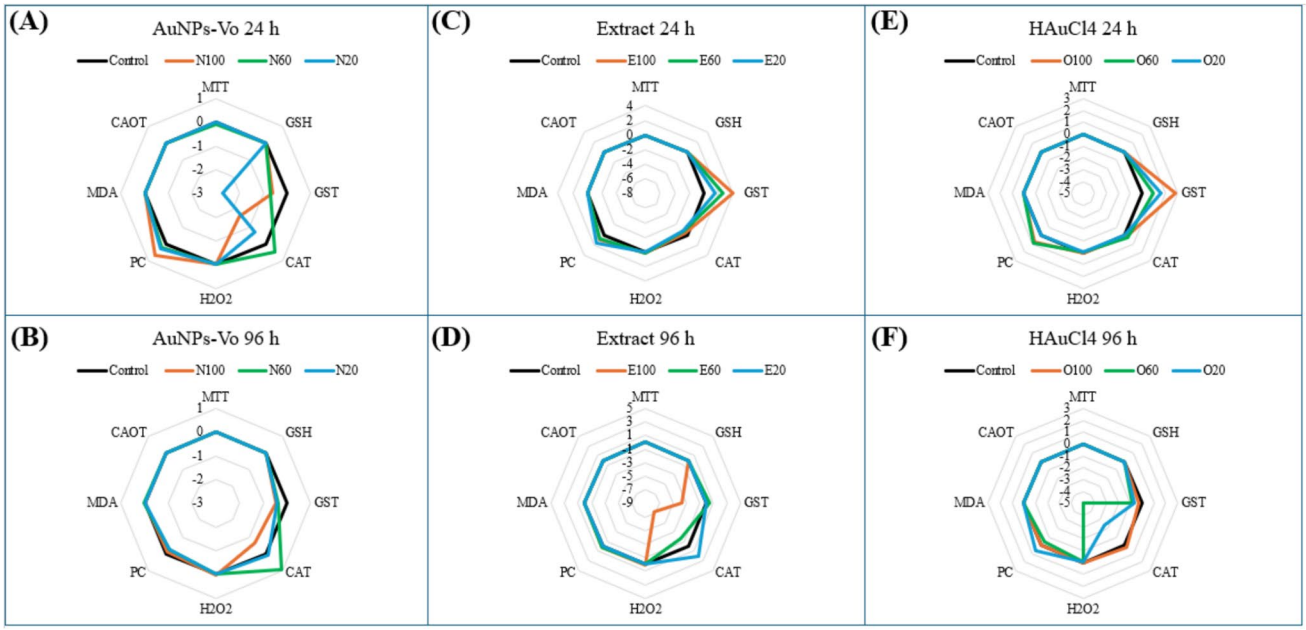


Fig. 15 Integrated Biomarker Response version 2 (IBRv2) radar plots showing oxidative stress and toxicity biomarker modulation in zebrafish exposed to AuNPs-Vo, plant extract, and $HAuCl_4$ at different concentrations after 24 and 96 h. Panels: (**A–B**) AuNPs-Vo; (**C–D**) extract; (**E–F**) HAuCl4. Biomarkers evaluated were MTT, GSH, GST, CAT, H_2O_2, PC, MDA, and CAOT. Data were standardized relative to control and plotted using biologically oriented signed values. Final IBRv2 scores were calculated as the sum of absolute biomarker deviations using Microsoft Excel

condition in which nanoparticle or extract components remain sufficiently bioavailable to induce oxidative imbalance, as supported by the contribution of GSH, MDA, and CAT to sample separation. In contrast, the comparatively lower toxicity observed for E100 may be associated with concentration-dependent physicochemical changes, such as aggregation, enhanced biomolecule adsorption, or altered protein corona formation, potentially reducing effective cellular interaction. Similar non-monotonic responses have been reported in plant-mediated Au-NPs systems, where intermediate concentrations can exhibit greater biological activity than more concentrated formulations.

Samples on the left (low Dim1) exhibit low values for variables on the right and high values for variables opposing Dim1, such as carbonylation, likely corresponding to N60 and N20 cells at 24 h. Finally, the darkest blue points likely represent control samples or treatments with a less pronounced GSH or CAT response, as seen for cells exposed to N100 at both time points and O60 at 96 h.

Oxidative stress biomarkers correlations from Integrated Biomarker Response version 2 (IBRv2)

The Integrated Biomarker Response version 2 (IBRv2) analysis revealed distinct biomarker modulation patterns according to treatment, concentration, and exposure time (Fig. 15). To preserve the biological directionality of biomarker responses, signs were assigned according to the expected toxicological meaning of each endpoint. For IBRv2 calculation, absolute values were summed to avoid cancellation between antagonistic responses and estimate the overall magnitude of biological disturbance.

For biosynthesized AuNPs (AuNPs-Vo), exposure for 24 h (Fig. 15A) induced moderate biomarker disturbance, with the highest IBRv2 observed for N20 (3.78), followed by N100 (2.99) and N60 (1.53). The N20 group was mainly characterized by a pronounced negative deviation in GST, suggesting early disruption of detoxification pathways, whereas N60 exhibited a more balanced profile with positive CAT modulation, indicating a more adaptive antioxidant response. After 96 h (Fig. 15B), the global biological disturbance decreased for all nanoparticle groups, particularly for N20 (0.81), while N60 showed the highest IBRv2 at this time point (1.60), mainly due to CAT elevation. These findings suggest that AuNPs-Vo induced only moderate and transient oxidative stress, with evidence of physiological adaptation after prolonged exposure.

For the plant extract alone, exposure induced stronger biomarker perturbations than AuNPs. After 24 h (Fig. 15C), IBRv2 values followed the concentration-dependent pattern E100 (5.46) > E60 (4.26) > E20 (3.81), largely driven by positive GST and proteins carbonilation (PC) modulation, indicating activation of antioxidant and detoxification mechanisms. However, after 96 h (Fig. 15D), E100 exhibited the highest IBRv2 value of the entire study (11.21), indicating severe global physiological disturbance. This

effect was mainly associated with marked negative deviations in CAT (-7.28) and GST (-3.57), suggesting antioxidant system exhaustion or metabolic imbalance after prolonged exposure to the highly concentrated extract. In contrast, E60 (2.46) and E20 (2.05) showed considerably lower disturbance, indicating a non-linear concentration-response relationship.

Finally, for $HAuCl_4$, moderate biological disturbance was observed after 24 h (Fig. 15E), with IBRv2 values decreasing with concentration dilution: O100 (3.80) > O60 (2.30) > O20 (1.75). This pattern was primarily associated with strong GST induction, suggesting activation of detoxification pathways in response to ionic gold exposure. After 96 h (Fig. 15F), however, a marked non-monotonic response was observed, with O60 presenting the highest IBRv2 (6.32), followed by O20 (3.75), whereas O100 displayed minimal disturbance (0.59). The O60 group showed strong negative CAT modulation (-4.99), indicating pronounced oxidative imbalance and confirming concentration-dependent toxicity that does not follow a linear dose-response pattern.

Overall, IBRv2 analysis demonstrated that biosynthesized AuNPs induced lower global biological disturbance than both the precursor salt and plant extract, supporting their improved biocompatibility. The plant extract alone showed concentration- and time-dependent effects, with severe perturbation under prolonged exposure at high concentration $HAuCl_4$ induced marked oxidative imbalance, particularly at intermediate concentration after 96 h, reinforcing the importance of nanoparticle synthesis in reducing the biological reactivity of gold ions.

The lower IBRv2 values observed for biosynthesized AuNPs compared with $HAuCl_4$ support the hypothesis that green synthesis improves nanoparticle biocompatibility by reducing the reactivity of free gold ions and promoting stabilization by phytochemical capping agents. Similar findings were reported by Machado et al. [59] who demonstrated reduced toxicity of biosynthesized AuNPs in zebrafish embryos compared with isolated extract conditions. Likewise, Ramachandran et al. [71] described relatively low oxidative stress and improved safety profiles for biologically synthesized AuNPs in adult zebrafish. In contrast, the elevated IBRv2 observed for E100 after 96 h suggests that prolonged exposure to highly concentrated extract may overwhelm antioxidant defenses, resulting in metabolic imbalance or pro-oxidant effects despite the presence of bioactive phytochemicals. This phenomenon has been previously associated with concentration-dependent dual antioxidant/pro-oxidant behavior of plant-derived compounds [50] . Additionally, the non-monotonic response observed for $HAuCl_4$, particularly the high disturbance in O60 after 96 h, may reflect differences in ionic bioavailability, uptake kinetics, or aggregation dynamics, as frequently described in nanotoxicology studies.

Conclusion

This study demonstrated the green synthesis of gold nanoparticles using an aqueous sap extract of *Virola oleifera* combined with factorial experimental design to identify the main variables controlling nanoparticle formation. The optimized synthesis conditions produced predominantly spherical AuNPs with nanometric size, negative surface charge, and high colloidal stability. The results highlight the importance of characterizing nanoparticles synthesized from freshly collected plant material, since seasonal variations may alter the concentration of secondary metabolites and affect nanoparticle formation. Physicochemical characterization confirmed the participation of phytochemicals from the extract in both Au^{3+} ion reduction and nanoparticle stabilization. Chromatographic and spectroscopic analyses revealed the presence of phenolic compounds, polyols, and flavonoids associated with the nanoparticle surface, supporting their stabilizing role. The surface charge of AuNPs also contributes to maintaining protonated or deprotonated states of adsorbed phytomolecules, influencing colloidal stability under different ionic and pH conditions. Biological assays showed that AuNPs-Vo exhibited low cytotoxicity inVero cells and did not significantly alter oxidative stress biomarkers at the tested concentrations. Overall, AuNPs-Vo fulfilled the main criteria of green synthesis, representing a sustainable, non-toxic nanomaterial with potential for reproducible plant-mediated nanotechnology applications.

Supplementary Information The online version contains supplementary material available at https://doi.org/10.1007/s41204-026-00576-3.

Acknowledgements This study was financed in part by the Coordination for the Improvement of Higher Education Personnel – Brazil (CAPES) – Finance Code 001. Thanks are due to Maria Carolina Peixoto Rodrigues for help in in supplementing and purifying the culture medium, performed cell passaging, prepared reagents (including MTT and adjustments of extract and NP concentrations), and during the initial MTT assay procedures. EMS acknowledges funding from the "Jovem Cientista do Nosso Estado" program, grated by the Research Support Foundation of the State of Rio de Janeiro (FAPERJ - Project E-26/204.405/2024 and E-26/211.268/2021) as well as support from the National Council for Scientific and Technological Development (CNPq 303248/2024-6).

Author contribution Rafaella de Resende Marques: Investigation, Formal analysis, Writing - Original Draft; Marcelo Raul Romero Tappin: Formal analysis, Writing - Review & Editing; Licinio Fontoura: Formal analysis; Virginia Garcia Correia: Formal analysis; Marcio Soares: Formal analysis; Daniel Adesse: Investigation, Methodology, Formal analysis; Writing - Review & Editing; Ana Maria Percebom Sette da Silva: Formal analysis; Writing - Review & Editing; Francc-

esca Fornasier: Formal analysis; Writing - Review & Editing; Mariana Gisbert Jardim dos Santos: Formal analysis; Tommaso Del Rosso: Writing - Review & Editing; Rachel Ann Hauser-Davis: Resources, Funding acquisition, Writing - Review & Editing, Supervision; Enrico Mendes Saggioro: Conceptualization, Resources, Writing - Review & Editing, Supervision, Project administration, Funding acquisition.

Funding The Article Processing Charge (APC) for the publication of this research was funded by the Coordenação de Aperfeiçoamento de Pessoal de Nível Superior - Brasil (CAPES) (ROR identifier: 00x0ma614). Fundação Carlos Chagas Filho de Amparo à Pesquisa do Estado do Rio de Janeiro,E-26/204.405/2024,Conselho Nacional de Desenvolvimento Científico e Tecnológico,303248/2024-6

Data availability No datasets were generated or analysed during the current study.

Declarations

Competing interests The authors declare no competing interests.

AI statement The authors used ChatGPT] for language enhancement and grammar check. Following AI assistance, the authors reviewed and edited the content as needed and take full responsibility for the content of this publication.

Ethics approval and consent to participate All authors have read, understood, and have complied as applicable with the statement on "Ethical responsibilities of Authors" as found in the Instructions for Authors.

Open Access This article is licensed under a Creative Commons Attribution 4.0 International License, which permits use, sharing, adaptation, distribution and reproduction in any medium or format, as long as you give appropriate credit to the original author(s) and the source, provide a link to the Creative Commons licence, and indicate if changes were made. The images or other third party material in this article are included in the article's Creative Commons licence, unless indicated otherwise in a credit line to the material. If material is not included in the article's Creative Commons licence and your intended use is not permitted by statutory regulation or exceeds the permitted use, you will need to obtain permission directly from the copyright holder. To view a copy of this licence, visit http://creativecommons.org/licenses/by/4.0/.

References

1. Khalil AHPS et al (2014) Production and modification of nanofibrillated cellulose using various mechanical processes: a review. Carbohydr Polym 99:649–665
2. Ahmad S et al (2022) Green synthesis of gold nanoparticles using *Delphinium chitralense* tuber extracts, their characterization and enzyme inhibitory potential. Braz J Biol 82:e257622
3. Albanese A, Chan WC (2011) Effect of gold nanoparticle aggregation on cell uptake and toxicity. ACS Nano 5(7):5478–5489
4. Alexieva V et al (2001) The effect of drought and ultraviolet radiation on growth and stress markers in pea and wheat. Plant Cell Environ 24(12):1337–1344
5. Aljabali A et al (2018) Synthesis of gold nanoparticles using leaf extract of *Ziziphus zizyphus* and their antimicrobial activity. Nanomaterials 8(3):174
6. Allocati N, Masulli M, di Ilio C, Federici L (2018) Glutathione transferases: substrates, inhibitors and pro-drugs in cancer and neurodegenerative diseases. Oncogenesis 7(1):8
7. Aloke C, Onisuru OO, Achilonu I (2024) Glutathione S-transferase: A versatile and dynamic enzyme. Biochem Biophys Res Commun 734:150774
8. Araujo PS et al (2020) Molluscicidal activity of polyvinylpyrrolidone (PVP)-functionalized silver nanoparticles to *Biomphalaria glabrata*: implications for control of intermediate host snail of *Schistosoma mansoni*. Acta Trop 210:105644
9. Awad MA et al (2019) Green synthesis of gold nanoparticles: preparation, characterization, cytotoxicity, and antibacterial activities. Mater Lett 256:126608
10. Balasubramanian S, Kala SMJ, Pushparaj T (2020) Lurthu. biogenic synthesis of gold nanoparticles using jasminum auriculatum leaf extract and their catalytic, antimicrobial and anticancer activities. J Drug Deliv Sci Techno 57:101620
11. Barbosa KBF et al (2010) Estresse oxidativo: conceito, implicações e fatores modulatórios. Rev De Nutr 23(4):629–643
12. Barreca D, Trombetta D, Mandalari G et al (2021) Mechanisms of plant antioxidants action. Plants 10(1):35
13. Bastús NG (2011) Comenge, Joan; Puntes, víctor kinetically controlled seeded growth synthesis of citrate-stabilized gold nanoparticles of up to 200 nm: size focusing versus ostwald ripening. Langmuir 27(17):11098–11105
14. Bôa ISF et al (2015) Resin from *Virola oleifera* protects against radiocontrast-induced nephropathy in mice. PLoS ONE 10(12):e0144329
15. Botteon CEA, Silva LB, Ccana-Ccapatinta GV et al (2021) Biosynthesis and characterization of gold nanoparticles using Brazilian red propolis and evaluation of its antimicrobial and anticancer activities. Sci Rep 11:1974
16. Bumbrah GS, Sharma RM (2016) Raman spectroscopy – basic principle, instrumentation and selected applications for the characterization of drugs of abuse. Egypt J Forensic Sci 6(3):209–215
17. Calabrese EJ (2022) Dose-response features of hormesis: a fundamental concept in biology. Chem Res Toxicol 35(11):1891–1905
18. Capuzzi E et al (2022) Malondialdehyde as a candidate biomarker for bipolar disorder: a meta-analysis. Prog Neuro-Psychopharmacol Biol Psychiatry 113:110469
19. Chahardoli A et al (2018) Green approach for synthesis of gold nanoparticles from *Nigella arvensis* leaf extract and evaluation of their antibacterial, antioxidant, cytotoxicity and catalytic activities. Artif Cells Nanomed Biotechnol 46(3):579–588
20. Chahardoli A et al (2019) Biological applications of phytosynthesized gold nanoparticles using leaf extract of *Dracocephalum kotschyi*. J Biomed Mater Res Part A 107(3):621–630
21. Chai Y-C, Mieyal JJ (2023) Glutathione and glutaredoxin—key players in cellular redox homeostasis and signaling. Antioxidants 12(8):1553
22. Chen WC et al (2008) Prevalence and determinants of workplace violence of health care workers in a psychiatric hospital in Taiwan. J Occup Health 50(3):288–293
23. Cheng J et al (2013) Surface functionalized gold nanoparticles for drug delivery. J Biomed Nanotechnol 9(8):1362–1369
24. Chokkalingam M et al (2019) Facile synthesis of Au and Ag nanoparticles using fruit extract of *Lycium chinense* and their anticancer activity. J Drug Deliv Sci Technol 49:308–315
25. Clogston JD, Patri AK (2011) Zeta potential measurement. Meth Mol Biol 697:63–70
26. Contreras L et al (2020) High antioxidant activity and low toxicity of gold nanoparticles synthesized with *Virola oleifera*: an approach using design of experiments. Res Square
27. Cruz JN et al (2024) Analysis of chemical composition, antioxidant activity, and toxicity of essential oil from *Virola sebifera* aubl (Myristicaceae). Molecules 29(14):3431

28. de Aquino PEA et al (2019) The wound healing property of N-methyl-(2S,4R)-trans-4-hydroxy-L-proline from *Sideroxylon obtusifolium* is related to its anti-inflammatory and antioxidant actions. J Evid-Based Integr Med 24:2515690X19865166
29. de Resende Marques R et al (2023) In vitro antibacterial effects of gold nanoparticles synthesized with *Virola oleifera* on *Staphylococcus aureus* and *Pseudomonas aeruginosa* strains. BioNanoScience 13(3):900–910
30. Diksha D et al (2023) Antibacterial potential of gold nanoparticles synthesized from leaf extract of *Syzygium cumini* against multidrug-resistant urinary tract pathogens. Cureus
31. Dos Santos Corrêa A et al (2018) *Virola oleifera*-capped gold nanoparticles showing radical-scavenging activity and low cytotoxicity. Mater Sci Eng 91:853–858
32. Esterbauer H, Cheeseman KH (1990) Determination of aldehydic lipid peroxidation products: malonaldehyde and 4-hydroxynonenal. In: Methods in Enzymology. [S.l.] Elsevier, 186, p 407–421
33. Fadeel B, Farcal L, Hardy B et al (2018) Advanced tools for the safety assessment of nanomaterials. Nat Nanotechnol 13:537–543
34. Fávero LP, Fávero P (2016) Análise de dados: modelos de regressão com Excel®, Stata® e SPSS®. v. 1. Rio de Janeiro, Elsevier Brasil, 2016.
35. Fayaz AM et al (2010) Biogenic synthesis of silver nanoparticles and their synergistic effect with antibiotics: a study against gram-positive and gram-negative bacteria. Nanomed Nanotechnol Biolo Med 6(1):103–109
36. Fernandes WR et al (2012) Avaliação do estresse oxidativo em cavalos de trote através da mensuração de malondialdeído (MDA) e glutationa reduzida (GSH) eritrocitária. Pesq Vet Bras 32(7):677–680
37. Ferreira DM (2016) Biossíntese otimizada de nanopartículas. Trabalho acadêmico.
38. de Ferro CO et al (2010) Atividade da catalase no pulmão, rim e intestino delgado não isquemiado de ratos após reperfusão intestinal. Rev do Col Bras De Cir 37(1):31–38
39. Francisco V et al (2021) Evaluation of *Virola oleifera* activity in musculoskeletal pathologies: inhibition of human multiple myeloma cells proliferation and combination therapy with dexamethasone or bortezomib. J Ethnopharmacol 272:113932
40. Fulgencio Diego R, Moura do MS (2007) Metodologia científica: determinação da atividade antioxidante total em frutas pela captura do radical livre ABTS•+: comunicado técnico. Fortaleza: Embrapa
41. Ganesan RM, Gurumallesh Prabu H (2019) Synthesis of gold nanoparticles using herbal *Acorus calamus* rhizome extract and coating on cotton fabric for antibacterial and UV blocking applications. Arabian J Chem 12(8):2166–2174
42. Ghaffari-Moghaddam M, Hadi-Dabanlou R (2014) Plant mediated green synthesis and antibacterial activity of silver nanoparticles using *Crataegus douglasii* fruit extract. J Ind Eng Chem 20(2):739–744
43. Ghramh HA et al (2019) Synthesis of gold nanoparticles (AuNPs) using *Ricinus communis* leaf ethanol extract, their characterization and biological applications. Nanomaterials 9(5):765
44. Godipurge SS et al (2016) A facile and green strategy for the synthesis of Au, Ag and Au–Ag alloy nanoparticles using aerial parts of *R. hypocrateriformis* extract and their biological evaluation. Enzyme Microb Technol 95:174–184
45. Gopinath K, Gowri S, Karthika V et al (2014) Green synthesis of gold nanoparticles from fruit extract of *Terminalia arjuna*, for the enhanced seed germination activity of *Gloriosa superba*. J Nanostruct Chem 4:115
46. Góth L (1991) A simple method for determination of serum catalase activity and revision of reference range. Clin Chim Acta 196(2–3):143–151
47. Gruber S, Nickel A (2023) Toxic or not toxic? The specifications of the standard ISO 10993–5 are not explicit enough to yield comparable results in the cytotoxicity assessment of an identical medical device. Front Med Technol 5:1195529
48. Habig WH, Pabst MJ, Jakoby WB (1974) Glutathione S-transferases. J Biolo Chem 249(22):7130–7139
49. Hendel T et al (2014) In situ determination of colloidal gold concentrations with UV–Vis spectroscopy: limitations and perspectives. Anal Chem 86(22):11115–11124
50. Hutagalung RA, Simanjuntak K, Fauziah C et al (2024) Green synthesis of gold nanoparticles with *Manilkara zapota* leaf extract and its application as antibacterial agent. Res J Pharm Technol 17(11):5509–5514
51. International organization for standardization. Biological evaluation of medical devices — Part 5: Tests for in vitro cytotoxicity. Geneva: ISO.
52. Jesus WB et al (2020) Biomarcadores enzimáticos e histológicos em brânquias de *Ucides cordatus* (Linnaeus, 1763) indicativos de impactos ambientais em uma região portuária do nordeste do Brasil. Arquivo Bras De Med Vet Zootec 72(4):1413–1423
53. Jiménez Pérez ZE et al (2017) Ginseng-berry-mediated gold and silver nanoparticle synthesis and evaluation of their in vitro antioxidant, antimicrobial, and cytotoxicity effects on human dermal fibroblast and murine melanoma skin cell lines. Int J Nanomed 12:709–723
54. Joudeh N, Linke D (2022) Nanoparticle classification, physicochemical properties, characterization, and applications: a comprehensive review for biologists. J Nanobiotechnol 20(1):262
55. Kang JP et al (2017) Biosynthesis of gold and silver chloride nanoparticles mediated by *Crataegus pinnatifida* fruit extract: in vitro study of anti-inflammatory activities. Artificial Cells Nanomed Biotechnol
56. Keijok WJ et al (2019) Controlled biosynthesis of gold nanoparticles with *Coffea arabica* using factorial design. Sci Rep 9(1):16019
57. Li J, Kang R, Tang D (2021) Monitoring autophagy-dependent ferroptosis. In: Methods in Cell Biology. [S.l.] Elsevier, 165, p 163–176
58. Lin J et al (2014) Inhibition of autophagy enhances the anticancer activity of silver nanoparticles. Autophagy 10(11):2006–2020
59. Machado S, González-Ballesteros N, Gonçalves A, Magalhães L, Passos MSP, Rodríguez-Argüelles MC, Gomes AC (2021) Toxicity in vitro and in zebrafish embryonic development of gold nanoparticles biosynthesized using *Cystoseira* macroalgae extracts. Int J Nanomed 16:5017–5036
60. Marques de RR (2020) Nanopartículas de ouro reduzidas com *Virola oleifera* inibem o crescimento de *Staphylococcus aureus* e *Pseudomonas aeruginosa*. Trabalho acadêmico
61. Mesquita CS et al (2014) Simplified 2,4-dinitrophenylhydrazine spectrophotometric assay for quantification of carbonyls in oxidized proteins. Anal Biochem 458:69–71
62. Milaneze BA et al (2016) Facile synthesis of monodisperse gold nanocrystals using *Virola oleifera*. Nanoscale Res Lett 11(1):465
63. Mulvaney P (1996) Surface plasmon spectroscopy of nanosized metal particles. Langmuir 12(3):788–800
64. Muthukumar T et al (2016) Green synthesis of gold nanoparticles and their enhanced synergistic antitumor activity using HepG2 and MCF7 cells and its antibacterial effects. Proc Biochem 51(3):384–391
65. Nascimento-Dias BLB (2025) Espectroscopia Raman: uma revisão concisa a partir da Física Aplicada e seu uso em pesquisas de Astrobiologia. Rev Bras De Ensino De Física 47:e20250271
66. Palaniswamy S et al (2024) Biosynthesis of gold nanoparticles from *Martynia annua* aqueous leaves extract, its antioxidant potential and antimicrobial ability against selected wound pathogens. Inorg Chem Commun 170:113241

67. Pereira ACH et al (2017) Gastroprotective activity of the resin from *Virola oleifera*. Pharm Biolo 55(1):472–480
68. Peterson GL (1977) A simplification of the protein assay method of Lowry et al which is more generally applicable. Anal Biochem 83(2):346–356
69. Pizzino G, Irrera N, Cucinotta M et al (2017) Oxidative stress: harms and benefits for human health. Oxid Med Cell Longev 2017:8416763
70. Qais FA et al (2019) Antibacterial effect of silver nanoparticles synthesized using *Murraya koenigii* (L.) against multidrug-resistant pathogens. Bioinorg Chem Appl 2019:1–11
71. Ramachandran R, Krishnaraj C, Abhay kumar VK, Harper SL, Kalaichelvan PT, Yun SI (2018) In vivo toxicity evaluation of biologically synthesized silver nanoparticles and gold nanoparticles on adult zebrafish: a comparative study. 3 Biotech 8(10): 441
72. REPÚBLICA FEDERATIVA DO BRASIL. Medida Provisória nº 2.186-16, de 23 de agosto de 2001. Dispõe sobre o acesso ao patrimônio genético, a proteção e o acesso ao conhecimento tradicional associado. **Diário Oficial da União**, Brasília, DF, 23 ago. 2001.
73. Rodríguez-León E, Rodríguez-Vázquez BE, Martínez-Higuera A et al (2019) Synthesis of gold nanoparticles using *Mimosa tenuiflora* extract: assessments of cytotoxicity, cellular uptake, and catalysis. Nanoscale Res Lett 14:334
74. Rue EA, Rush MD, van Breemen RB (2018) Procyanidins: a comprehensive review encompassing structure elucidation via mass spectrometry. Phytochem Rev 17(1):1–16
75. Wang M, Carver JJ, Phelan VV, Sanchez LM, Garg N, Peng Y, Nguyen DD, Watrous J, Kapono CA, Luzzatto-Knaan T, Porto C, Bouslimani A (2016) Sharing and community curation of mass spectrometry data with global natural products social molecular networking. Nat Biotechnol 34:828–837
76. Sánchez W, Burgeot T, Porcher J-M (2013) A novel "Integrated Biomarker Response" calculation based on reference deviation concept. Environ Sci Pollut Res 20(5):2721–2725
77. Sharma TSK et al (2019) Biogenic fabrication of gold nanoparticles using *Camellia japonica* L. leaf extract and its biological evaluation. J Mater Res Technol 8(1):1412–1418
78. Sharmin S, Rahaman M, Sarkar C (2021) Nanoparticles as antimicrobial and antiviral agents: a literature-based perspective study. Heliyon 7
79. Silva LPC et al (2023) Cellulose nanofibers infused with pomegranate gold nanoparticles display antibacterial activity. NanoStruct Nano-Obj 36:101045
80. Silva VDM et al (2020) Bioactive activities and chemical profile characterization using paper spray mass spectrometry of extracts of Eriobotrya japonica Lindl leaves. Rapid Commun Mass Spectrom 34(19):e8883
81. Souto EB, Severino P, Santana MHA (2012) Preparação de nanopartículas poliméricas a partir da polimerização de monômeros: parte I. Polímeros 22(1):96–100
82. Uemura T, Ohba M, Kitagawa S (2004) Size and surface effects of prussian blue nanoparticles protected by organic polymers. Inorg Chem 43(23):7339–7345
83. Valotto RS, Keijok WJ, Guimarães MCC (2021) Síntese e caracterização de nanopartículas de ouro reduzidas com casca de romã (*Punica granatum* L.). In: Paniagua Cleiseano Emanuel da Silva (ed) O Ensino E A Pesquisa Em Química **3**.1edn. [S.l.]: Atena Editora, p 107–116
84. Vimalraj S, Ashokkumar T, Saravanan S (2018) Biogenic gold nanoparticles synthesis mediated by *Mangifera indica* seed aqueous extracts exhibits antibacterial, anticancer and anti-angiogenic properties. Biomed Pharmacother 105:440–448
85. Vinay SP, Udayabhanu, Nagaraju G, Chandrappa CP, Chandrasekhar N (2019) Novel Gomutra (cow urine) mediated synthesis of silver oxide nanoparticles and their enhanced photocatalytic, photoluminescence and antibacterial studies. J Sci Adv Mater Dev 4(3):392–399
86. Wadhwa M, Bakshi MPS, Makkar HPS (2016) Wastes to worth: value added products from fruit and vegetable wastes. CABI Rev :1–25
87. Wilhelm Filho D et al (2005) Effect of different oxygen tensions on weight gain, feed conversion, and antioxidant status in piapara, *Leporinus elongatus* (Valenciennes, 1847). Aquaculture 244(1–4):349–357
88. Chun-Gang Y et al (2017) Green synthesis of gold nanoparticles using *Citrus maxima* peel extract and their catalytic/antibacterial activities. IET Nanobiotechnol 11(5):523–530
89. Zhang Y et al (2023) The applications of nanozymes in neurological diseases: from mechanism to design. Theranostics 13(8):2492–2514
91. Rotimi L, Ojemaye MO, Okoh OO, Sadimenko A, Okoh AI (2019) Synthesis, characterization, antimalarial, antitrypanocidal and antimicrobial properties of gold nanoparticle. Green Chem Lett Rev 12(1):61–68

Publisher's Note Springer Nature remains neutral with regard to jurisdictional claims in published maps and institutional affiliations.

Authors and Affiliations

Rafaella de Resende Marques[1] · Marcelo Raul Romero Tappin[2] · Licinio Fontoura[2] · Virginia Garcia Correia[2] · Marcio Soares[2] · Daniel Adesse[3,4] · Ana Maria Percebom Sette da Silva[5] · Franccesca Fornasier[6] · Mariana Gisbert Jardim dos Santos[5] · Tommaso Del Rosso[5] · Rachel Ann Hauser-Davis[1] · Enrico Mendes Saggioro[1]

✉ Enrico Mendes Saggioro
enrico.saggioro@fiocruz.br

Rafaella de Resende Marques
rafaella.rafa90@gmail.com

Marcelo Raul Romero Tappin
marcelo.tappin@fiocruz.br

Licinio Fontoura
licinio.fontoura@fiocruz.br

Virginia Garcia Correia
virginia.correia@fiocruz.br

Marcio Soares
marcio.soares@fiocruz.br

Daniel Adesse
daniel.adesse@gmail.com

Ana Maria Percebom Sette da Silva
apercebom@puc-rio.br

Franccesca Fornasier
franccescafornasier@gmail.com

Mariana Gisbert Jardim dos Santos
marianagisbert@gmail.com

Tommaso Del Rosso
tommaso@puc-rio.br

Rachel Ann Hauser-Davis
rachel.hauser.davis@gmail.com

[1] Laboratório de Avaliação e Promoção da Saúde Ambiental, Oswaldo Cruz Foundation, Rio de Janeiro, Brazil

[2] Instituto de Tecnologia em Fármacos - Farmanguinhos, Oswaldo Cruz Foundation, Rio de Janeiro, Brazil

[3] Laboratório de Biologia Estrutural, Oswaldo Cruz Foundation, Rio de Janeiro, Brazil

[4] Laboratory of Ocular Immunology and Transplantation, University of Miami, Coral Gables, United States

[5] Pontifical Catholic University of Rio de Janeiro, Rio de Janeiro, Brazil

[6] Chemical Engineering Program, Federal University of Rio de Janeiro, Rio de Janeiro, Brazil